J. Fluid Mech. (2021), *vol*. 912, A36, doi:10.1017/jfm.2020.1138

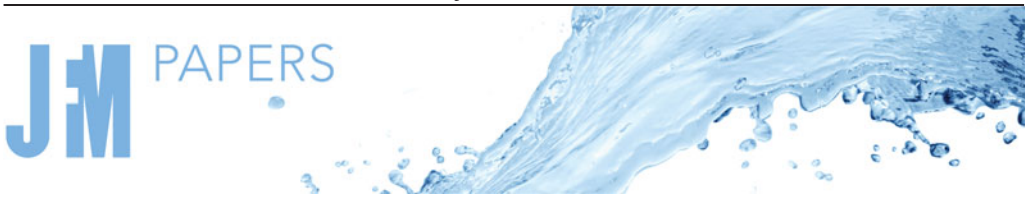

Interscale kinetic energy transfer in chemically reacting compressible isotropic turbulence

Jian Teng[1,2,3], **Jianchun Wang**[1,3,†], **Hui Li**[2] **and Shiyi Chen**[1,3,†]

[1]Guangdong Provincial Key Laboratory of Turbulence Research and Applications, Center for Complex Flows and Soft Matter Research, Department of Mechanics and Aerospace Engineering, Southern University of Science and Technology, Shenzhen, Guangdong 518055, PR China

[2]School of Power and Mechanical Engineering, Wuhan University, Wuhan 430072, PR China

[3]Southern Marine Science and Engineering Guangdong Laboratory, Guangzhou 511458, PR China

(Received 13 May 2020; revised 5 October 2020; accepted 16 December 2020)

Interscale kinetic energy transfer in chemically reacting compressible isotropic turbulence is studied using numerical simulations at turbulent Mach numbers 0.2 and 0.8 for isothermal and exothermic reactions. At low turbulent Mach number $M_t = 0.2$ for exothermic reaction, heat release greatly enhances expansion and compression motions, and induces the formation of shocklets which are not observed for isothermal reaction at the same turbulent Mach number. It is found that heat release through exothermic reactions enhances both the positive and the negative components of pressure–dilatation, as well as positive and negative components of subgrid-scale (SGS) kinetic energy flux, indicating an increase of both forward-scatter and backscatter of kinetic energy. The SGS flux of kinetic energy has a tendency to be from large scales to small scales. The solenoidal components of pressure–dilatation and SGS kinetic energy flux are minorly influenced by heat release of reaction, while the dilatational components of pressure–dilatation and SGS kinetic energy flux are significantly intensified by heat release at all length scales. Heat release enhances the kinetic energy of the dilatational mode through the pressure work, and leads to the increase of dilatational kinetic energy transfer from large scales to small scales through dilatational SGS flux, as well as the viscous dissipation of dilatational kinetic energy at small scales. Taylor Reynolds number has a minor influence on the qualitative statistical properties of interscale kinetic energy transfer terms.

Key words: compressible turbulence, isotropic turbulence, turbulent reacting flows

† Email addresses for correspondence: wangjc@sustech.edu.cn, chensy@sustech.edu.cn

1. Introduction

Turbulence–chemistry interaction is a complex physicochemical phenomenon which is widely observed in combustion devices, oil burners and aerospace propulsion systems (Libby & Williams 1981; Peters 2000; Kuo & Acharya 2012). The intricate phenomenon of the turbulence–chemistry interaction involves complex flow dynamics and energy transfer in a wide range of spatial and temporal scales (Jaberi & Madnia 1998; Livescu, Jaberi & Madnia 2002; Paes & Xuan 2018). Understanding the fundamental mechanisms of turbulence-chemistry interaction is helpful in combustion engine design, efficient energy utilization and combustor pollutant control (Gao & Obrien 1991; Leonard & Hill 1992; Jaberi *et al.* 1996; Barths, Hasse & Peters 2000; Peters 2000; Wu *et al.* 2010).

Early computational studies on turbulence–chemistry interaction provided meaningful results on the complicated coupling mechanisms between turbulent motion and chemical reactions through extensive direct numerical simulations (DNS) of forced, decay and shear chemically reacting turbulence (Jaberi & James 1999; Martín & Candler 1999; Jaberi, Livescu & Madnia 2000; Knaus & Pantano 2009; Duan & Martín 2011; Chen & Li 2013). It was found that non-uniform heat release through chemical reactions can greatly intensify pressure, density and temperature fluctuations (Balakrishnan, Sarkar & Williams 1995; Jaberi & Madnia 1998) and thus lead to an increase of compression and expansion motions at all length scales (Eschenroeder 1964; Jaberi *et al.* 2000; Paes & Xuan 2018). Moreover, turbulence can enhance the transfer of reactants and products, and consequently affects the dynamics of chemical reaction as well as the structures of the reaction zone (Hill 1976; Leonard *et al.* 1988; Leonard & Hill 1992; Hamlington, Poludnenko & Oran 2011).

Investigation of energy transfer within the reacting system is helpful in understanding the interaction mechanism in reacting turbulence. Jaberi & Madnia (1998) analysed weakly compressible reacting isotropic turbulence through a DNS database and found that energy from chemical reactions is basically transferred to dilatational component of kinetic energy through pressure work, and is further transferred from the dilatational component to the solenoidal part through the advection process. Livescu *et al.* (2002) studied the exchange of kinetic energy and internal energy in non-premixed reacting compressible homogeneous shear turbulence and found that, during the reaction process, the dilatational part of kinetic energy production increases due to heat release. The pressure–dilatation correlation is responsible for the transfer of internal energy to kinetic energy. Meanwhile, the kinetic energy decreases in the direction of the mean velocity, and increases in the direction of the shear stress during the intense reaction period. The above works provided meaningful insight into energy transfer between internal energy and kinetic energy from a volumetric average perspective for reacting weakly compressible isotropic and shear reacting turbulence. The transfer of kinetic energy among different length scales in reacting turbulence remains to be explored.

The analysis of interscale kinetic energy transfer provides an effective approach to understanding the local behaviour of energy transfer beyond the statistically average sense. The interscale transfer of kinetic energy can be described by the classical energy-cascade hypothesis (Pope 2000; Richardson & Lynch 2007), which is known as forward-scatter energy cascade in the sense of statistics: kinetic energy has a statistical tendency to be generated at the largest scales and then transferred progressively to smaller scales and finally dissipated by molecular viscosity nearly at Kolmogorov length scales (Pope 2000; Goto 2008; Sagaut & Cambon 2008; Aluie 2011; Aluie, Li & Li 2012; Aluie 2013; Wang *et al.* 2013*a*, 2018*a*; Eyink & Drivas 2018; Yasuda & Vassilicos 2018). In three-dimensional incompressible turbulence, the forward-scatter of kinetic energy is known to prevail (Pope 2000; Sagaut & Cambon 2008; O'Brien *et al.* 2017). On the other hand, the opposite

kinetic energy transfer, namely, the energy backscatter has been largely observed in both reacting and non-reacting compressible turbulence (Leslie & Quarini 1979; Piomelli *et al.* 1991; Domaradzki & Saiki 1997; Ishihara, Gotoh & Kaneda 2009; Cardesa *et al.* 2015). For weak and moderate compressible reacting turbulence, energy backscatter is widely observed in flame brush and expansion regions where reaction heat release is strong. Urzay *et al.* (2013) and O'Brien *et al.* (2014) studied the dynamics of backscatter of kinetic energy in reacting H_2–air turbulent mixing layers. They reported that backscatter of kinetic energy occurs primarily in expansion regions. Through analysing a DNS database of turbulent premixed flame, O'Brien *et al.* (2017) investigated the kinetic energy transfer between turbulence and flames, and observed the transfer of kinetic energy from small scales to large scales in the flame brush. They also found that small amounts of enthalpy created by combustion heat release are transformed into small-scale kinetic energy by means of the subgrid-scale (SGS) pressure-gradient velocity correlation, and the resulting overload of SGS kinetic energy is transferred to the resolved scales through SGS backscatter. The underlying mechanism for kinetic energy backscatter in reacting compressible turbulence requires further exploration. Towery *et al.* (2016) analysed the spectral kinetic energy transfer by advection in turbulent premixed reacting flows and concluded that advective processes transfer energy from small to large scales in the flame brush and the net up-scale transfer of energy occurs primarily at spatial scales near the laminar flame thermal width. Paes & Xuan (2018) analysed the temporal evolution of kinetic energy of a chemically reacting *n*-heptane and air mixture in compressible homogeneous isotropic turbulence and found that kinetic energy can be transferred from small scales to large scales in chemically reacting turbulence through pressure–dilatation work at the flame front. The energy budget analysis (Kim *et al.* 2018) further revealed that energy is extracted by mean pressure-gradient interscale flux at characteristic flame scales and then injected into both larger scales and smaller scales.

For highly compressible chemically reacting turbulence, the compressibility effect and reaction heat release further complicate the interscale energy transfer process. The presence of shocklets in highly compressible turbulence considerably increases flow dilatation at small scales which significantly enhances interscale kinetic energy transfer as well as energy dissipation (Lee, Lele & Moin 1991; Samtaney, Pullin & Kosović 2001). Wang *et al.* (2013*a*, 2018*a*) studied the interscale kinetic energy transfer in highly compressible non-reacting isotropic turbulence and found that the increase of flow compressibility enhances both kinetic energy forward-scatter and backscatter. The dilatational mode can dominate over the solenoidal mode in kinetic energy transfer with the increase of flow compressibility. Nevertheless, heat release effects through chemical reactions on interscale kinetic energy transfer in highly compressible turbulence are less understood due to the intricate combined influence of compressibility and heat release.

This study aims to explore the interscale transfer of kinetic energy in solenoidally forced stationary chemically reacting compressible isotropic turbulence and address the effects of flow compressibility and heat release on the interscale kinetic energy transfer. The rest of the paper is organized as follows. In § 2, the governing equations are presented and the numerical method is described. The one-point statistics and reaction characteristics of the simulated chemically reacting flows are presented in § 3. The dynamical equations for the filtered kinetic energy are introduced in § 4. In § 5, results on interscale transfer of kinetic energy are analysed and discussed. The effects of Taylor Reynolds number on interscale transfer of kinetic energy are presented in § 6. Major findings and conclusions are summarized in § 7.

2. Governing equations and numerical method

Numerical simulations of solenoidally forced stationary chemically reacting compressible isotropic turbulence are performed, employing the following dimensionless Navier–Stokes equations in conservative form:

$$\frac{\partial \rho}{\partial t} + \frac{\partial \left(\rho u_j\right)}{\partial x_j} = 0, \tag{2.1}$$

$$\frac{\partial \left(\rho u_i\right)}{\partial t} + \frac{\partial \left[\rho u_i u_j + p\delta_{ij}\right]}{\partial x_j} = \frac{1}{Re}\frac{\partial \sigma_{ij}}{\partial x_j} + \mathcal{F}_i, \tag{2.2}$$

$$\frac{\partial \mathcal{E}}{\partial t} + \frac{\partial \left[(\mathcal{E}+p)u_j\right]}{\partial x_j} = \frac{1}{\alpha}\frac{\partial}{\partial x_j}\left(\kappa\frac{\partial T}{\partial x_j}\right) + \frac{1}{Re}\frac{\partial \left(\sigma_{ij}u_i\right)}{\partial x_j} + Q - \Lambda + \mathcal{F}_j u_j, \tag{2.3}$$

$$\frac{\partial (\rho Y_s)}{\partial t} + \frac{\partial \left(\rho Y_s u_j\right)}{\partial x_j} = \frac{1}{Re}\frac{1}{Sc}\frac{\partial}{\partial x_j}\left(\mu\frac{\partial Y_s}{\partial x_j}\right) + \dot{\omega}_s, \quad s = 1, 2, \ldots, n_s - 1, \tag{2.4}$$

$$p = \rho T / \left(\gamma M^2\right), \tag{2.5}$$

where u_i is the velocity component, p is the pressure, T is the temperature and ρ is the mixture density. The viscous stress σ_{ij} is given by

$$\sigma_{ij} = \mu\left(\frac{\partial u_i}{\partial x_j} + \frac{\partial u_j}{\partial x_i}\right) - \frac{2}{3}\mu\theta\delta_{ij}, \tag{2.6}$$

where, $\theta = \partial u_k/\partial x_k$ is the velocity divergence. For the multispecies mixture, Y_s denotes the mass fraction of the sth species, $\dot{\omega}_s$ is production rate of the sth species and n_s is the total number of species. Here Q denotes total heat of reaction.

The total energy per unit volume $\mathcal{E}$ is defined by

$$\mathcal{E} = \frac{p}{\gamma - 1} + \frac{1}{2}\rho\left(u_j u_j\right). \tag{2.7}$$

A set of reference scales are used to normalize the variables in chemically reacting compressible turbulence, including the reference length L_f, velocity U_f, density ρ_f, pressure $p_f = \rho_f U_f^2$, temperature T_f, energy per unit volume $\rho_f U_f^2$, viscosity μ_f and thermal conductivity κ_f. Three reference governing parameters are derived: the reference Reynolds number $Re = \rho_f U_f L_f/\mu_f$; the reference Mach number $M = U_f/c_f$; and the reference Prandtl number $Pr = \mu_f C_p/\kappa_f$. The speed of sound is defined by $c_f = \sqrt{\gamma R T_f}$, where R is the specific gas constant and $\gamma = C_p/C_v$ is the ratio of specific heat at constant pressure C_p to that at constant volume C_v. Here γ is assumed to be equal to 1.4 in our simulations. The parameter α is defined by $\alpha = PrRe(\gamma - 1)M^2$. The Schmidt number $Sc = \mu_f/\rho_f\mathcal{D}_f$, where $\mathcal{D}_f$ is mass diffusivity proportional to $T_f^{3/2}/p_f$ for gas. It is assumed that the parameters $Pr = Sc = 0.7$, and the gas is calorically perfect (Jaberi & James 1999; Jaberi *et al.* 2000; Wang *et al.* 2010).

Sutherland's law is adopted for calculation of the non-dimensional temperature-dependent viscosity coefficient μ and thermal conductivity coefficient κ (Wang *et al.* 2010)

as follows:

$$\mu = \frac{1.4042T^{1.5}}{T + 0.40417}, \tag{2.8}$$

$$\kappa = \frac{1.4042T^{1.5}}{T + 0.40417}. \tag{2.9}$$

The large-scale forcing $\mathcal{F}_i$ is applied to the solenoidal velocity component by fixing the velocity spectrum within the two lowest wavenumber shells (Chen & Cao 1997; Wang *et al.* 2010; Donzis & Maqui 2016). The spatially uniform thermal cooling Λ is utilized to sustain the internal energy in a statistically steady state (Wang *et al.* 2010).

An Arrhenius type single-step irreversible reaction equation is adopted to evaluate the chemical reaction source terms and reaction heat release (Jaberi & James 1999; Jaberi *et al.* 2000),

$$A + rB \rightarrow (1 + r)P, \tag{2.10}$$

where, A and B denote two reactants and P is the product. In the current study, $r = 1$ is considered. The mass fractions and the reaction rates of species A, B, P are denoted by Y_A, Y_B, Y_P and $\dot{\omega}_A$, $\dot{\omega}_B$, $\dot{\omega}_P$, respectively. Reaction rates of reactants and product are given by

$$\dot{\omega}_A = \dot{\omega}_B = -\tfrac{1}{2}\dot{\omega}_P = -Da\rho^2 Y_A Y_B \exp(-Ze/T), \tag{2.11}$$

where the Damköhler number $Da = K_f \rho_f L_f / U_f$ and the Zeldovich number $Ze = E_a/RT_f$. Here K_f is the reaction rate parameter, which is assumed constant, and E_a is the activation energy (Jaberi & James 1999; Jaberi *et al.* 2000).

The heat source term Q is given by

$$Q = \frac{Ce}{(\gamma - 1)M^2}\dot{\omega}_P, \tag{2.12}$$

where the heat release parameter $Ce = -H^0/C_p T_f$ and $-H^0$ is the heat of reaction. It can be noted that the species production rate is determined by Da and Ze. The above two parameters in combination with Ce determine the heat generation rate (Jaberi & James 1999; Jaberi *et al.* 2000).

The governing equations of chemically reacting compressible turbulence are solved numerically in a cubic domain of $(2\pi)^3$ by using periodic boundary conditions in all three spatial directions. A hybrid scheme combining an eighth-order compact finite difference scheme for smooth regions and a seventh-order weighted essentially non-oscillatory (known as WENO) scheme (Balsara & Shu 2000) for shock regions (Wang *et al.* 2010, 2011, 2012*a*) is adopted for both weakly and highly compressible reacting isotropic turbulence. To implement the shock detecting process, a shock front detecting relation $\theta < -R_\theta \theta'$ (Samtaney *et al.* 2001) is used, where, $R_\theta = 3.0$. Then, the shock front and additional six grid points on both left and right in each spatial direction immediately outside the shock front are treated as the shock region that is calculated by the weighted essentially non-oscillatory scheme. The remaining region is defined as the smooth region (Wang *et al.* 2010). For weakly compressible turbulence without shocklets, the entire computational domain is treated as the smooth region. Successful applications of this numerical scheme are referred to in Wang *et al.* (2012*a*,*b*, 2013*a*,*b*, 2018*a*,*b*, 2020).

The simulation process comprises two consecutive steps. In the first step, the source terms and reaction heat term are turned off for development of non-reacting multispecies

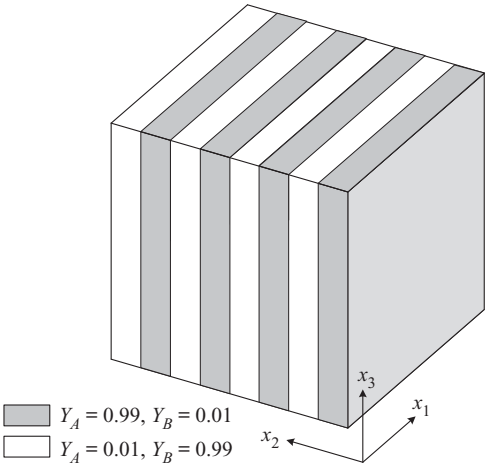

Figure 1. Initial density field at the start of chemical reaction.

compressible turbulence. The velocity field is driven and maintained by a large-scale momentum forcing. The kinetic energy cascade from large to small scales requires energy input through forcing at the large scales, to balance the viscous dissipation at the small scales. At the same time, the viscous dissipation is converted to thermal energy or heating at the small scales. A spatially uniform cooling function is applied to keep the average internal energy in a steady state (Wang *et al.* 2010). When the non-reacting compressible turbulence reaches a statistically steady state, the velocity and temperature are used as the initial values for the next step. The aim for step one is to get a steady state velocity and temperature field in which the large-scale forcing and cooling are in balance. In the second step, the source terms and reaction heat term are switched on for the chemical reaction and the density field is reinitialized in the way illustrated in figure 1. The focus in step two is species variation, reaction heat release and the interaction with turbulent motion. The initial density field has unity volume average value and no turbulent fluctuations. In the x_1–x_3 planes, the initial mass fraction values of Y_A and Y_B at every grid point are equal and constant. The domain in the x_2 direction is uniformly divided into eight segments: $Y_A = 0.99$, $Y_B = 0.01$ in the 1st, 3rd, 5th, 7th segments, and $Y_A = 0.01$, $Y_B = 0.99$ in the 2nd, 4th, 6th, 8th segments. The spatial average of both Y_A and Y_B are equal to 0.5, and Y_P is zero over the entire domain. Details of the scalar initialization are referred to in Jaberi *et al.* (1996). It should be noted that Jaberi & Livescu *et al.* used random scalar initialization with double-delta probability density function (p.d.f.) distribution (Jaberi & James 1999; Livescu *et al.* 2002) and scalar slabs initialization (Jaberi *et al.* 2000) in simulating non-premixed compressible isotropic, decaying and shear reacting turbulence and found that when the simulation time is long enough, the conserved scalar variance is small. Teng *et al.* (2020) analysed the influence of multispecies density initialization using similar slabs with different slab widths on flow statistics. The numerical results suggested that the slab initialization method for multispecies density field has minor influence on flow statistics at the initial chemical reaction phrase, and the results based on statistically steady state flow data when chemical reactions are almost finished are nearly unaffected by initial density field. Thus, the subsequent statistical analysis are based on flow data with a long development time to avoid the influence of initial scalar distribution.

Resolution	Re_λ	M_t	Da	Ze	Ce	$\eta/\Delta x$	L_I/η	S_3	ϵ_0	$-\langle p\theta\rangle$	$-\langle p\theta\rangle/\epsilon_0$
512^3	158	0.2	2	0	0	0.98	120	−0.51	0.75	-1.8×10^{-3}	-2.4×10^{-3}
512^3	158	0.2	200	8	3	1.03	117	−0.81	0.64	-5.7×10^{-2}	-8.9×10^{-2}
512^3	162	0.8	2	0	0	1.02	118	−0.81	0.67	8.3×10^{-3}	1.2×10^{-2}
512^3	156	0.8	200	8	3	1.00	117	−1.32	0.72	1.9×10^{-2}	2.6×10^{-2}

Table 1. Specification of DNS parameters and resulting flow statistics.

3. One-point statistics and reaction characteristics of chemically reacting compressible isotropic turbulence

The statistical analysis of chemically reacting compressible isotropic turbulence depends on two vital parameters: the Taylor microscale Reynolds number Re_λ and the turbulent Mach number M_t, which are defined, respectively, by Wang *et al.* (2018*b*) as

$$Re_\lambda = Re\frac{\langle\rho\rangle u'\lambda}{\sqrt{3}\langle\mu\rangle}, \quad M_t = M\frac{u'}{\langle\sqrt{T}\rangle}, \tag{3.1a,b}$$

where $\langle\rangle$ stands for spatial average. The root mean square (r.m.s.) velocity magnitude is $u' = \sqrt{\langle u_1^2 + u_2^2 + u_3^2\rangle}$ and the Taylor microscale is

$$\lambda = \sqrt{\frac{\langle u_1^2 + u_2^2 + u_3^2\rangle}{\langle(\partial u_1/\partial x_1)^2 + (\partial u_2/\partial x_2)^2 + (\partial u_3/\partial x_3)^2\rangle}}. \tag{3.2}$$

Two sets of reaction parameters are employed to represent different reaction rate and heat release rate. The set ($Da = 2$, $Ze = 0$, $Ce = 0$) defines an isothermal reaction and the other set ($Da = 200$, $Ze = 8$, $Ce = 3$) represents the exothermic reaction. The specification of simulated parameters and resulting flow statistics are listed in table 1. Simulations are performed on a grid with a resolution of 512^3 at initial Taylor Reynolds number 400 and at turbulent Mach numbers $M_t = 0.2$ and 0.8. The Kolmogorov length scale is defined by $\eta = [\langle\mu/(Re\rho)\rangle^3/\langle\epsilon_V/\rho\rangle]^{1/4}$, where the dissipation rate per unit volume is given by $\epsilon_V = \sigma_{ij}\mathcal{S}_{ij}/Re$ and the strain rate tensor $\mathcal{S}_{ij}$ is defined by $\mathcal{S}_{ij} = (1/2)(\partial u_i/\partial x_j + \partial u_j/\partial x_i)$. The magnitude of Kolmogorov length scale η represents the dissipation-range resolution, which plays a significant role in the grid convergence of velocity statistics in DNS (Watanabe & Gotoh 2007).

As shown in table 1, the resolution parameter $\eta/\Delta x$ lies within the range between 0.98 and 1.03, where Δx denotes the gridding length in each direction. It is straightforward to derive that $3.08 < k_{max}\eta < 3.23$ where the largest wavenumber k_{max} is half of the number of grids N in each direction: $k_{max} = N/2 = \pi/\Delta x$. Previous DNS results (Donzis & Maqui 2016; Wang, Gotoh & Watanabe 2017) showed that the resolution parameter $\eta/\Delta x \geqslant 0.5$ is good enough for convergence of high-order moments of velocity gradients. For high turbulent Mach number $M_t = 0.8$, the resolution parameter $\eta/\Delta x \geqslant 1.0$. Therefore, the overall statistics should be well converged in current numerical simulations (Wang *et al.* 2011, 2012*b*).

The integral length scale L_I is defined by

$$L_I = \frac{3\pi}{2\,(u')^2}\int_0^\infty \frac{E(k)}{k}\,\mathrm{d}k, \tag{3.3}$$

where $E(k)$ is the spectra of kinetic energy per unit mass, namely, $\int_0^\infty E(k)\,\mathrm{d}k = (u')^2/2$. The ratio of L_I/η lies within the range $117 \leqslant L_I/\eta \leqslant 120$ in current simulation cases.

The velocity derivative skewness S_3 is defined by

$$S_3 = \frac{\left[\left\langle(\partial u_1/\partial x_1)^3 + (\partial u_2/\partial x_2)^3 + (\partial u_3/\partial x_3)^3\right\rangle\right]/3}{\left\{\left\langle(\partial u_1/\partial x_1)^2 + (\partial u_2/\partial x_2)^2 + (\partial u_3/\partial x_3)^2\right\rangle/3\right\}^{3/2}}. \tag{3.4}$$

For isothermal reaction ($Da = 2$) at turbulent Mach numbers $M_t = 0.2$, the value of S_3 is similar to typical values of -0.6 to -0.4 in non-reacting weakly compressible turbulence (Wang *et al.* 2017). At $M_t = 0.8$ for isothermal reaction ($Da = 2$), the formation of shocklets in compressible turbulence results in a larger magnitude of S_3 (Wang *et al.* 2011, 2017). For exothermic reactions ($Da = 200$), magnitudes of S_3 are significantly enhanced at $M_t = 0.2$ and 0.8 due to strong heat release.

The average total dissipation rate of kinetic energy can be defined as $\epsilon_T = -\langle p\theta\rangle + \epsilon_0$ (Wang *et al.* 2012*a*, 2018*a*; Jagannathan & Donzis 2016), here $-\langle p\theta\rangle$ is the pressure–dilatation term and ϵ_0 is the viscous dissipation. Here ϵ_T represents the total conversion rate of kinetic energy into internal energy through pressure dilation and viscous dissipation. For isothermal reactions ($Da = 2$), $-2.4 \times 10^{-3} \leqslant -\langle p\theta\rangle/\epsilon_0 \leqslant 1.2 \times 10^{-2}$ at $M_t = 0.2$ and 0.8. The magnitude of $-\langle p\theta\rangle/\epsilon_0$ increases for exothermic reactions ($Da = 200$) at $M_t = 0.2$ and 0.8 compared with the value for isothermal reactions at the same turbulent Mach number.

The temporal variation of reaction statistics for isothermal ($Da = 2$) and exothermic ($Da = 200$) reactions at turbulent Mach number $M_t = 0.2$ and 0.8 is depicted in figure 2. The lines represent the results obtained with a previously developed zero-dimensional model (Teng *et al.* 2020). In the zero-dimensional model, chemical reaction occurs in an ideal point without flow motion. The initial species mass fraction for A, B and P are 0.5, 0.5 and 0.0, respectively. Both the initial density and temperature are 1.0 which are identical to the average initial values for DNS simulations. For isothermal ($Da = 2$) reactions as shown in figure 2(*a*), the temporal variation of mass fraction for reactant A and product P at turbulent Mach number $M_t = 0.2$ and 0.8 nearly collapse with the zero-dimensional results. For exothermic ($Da = 200$) reactions as shown in figure 2(*b*), the reactant consumption rate and product generation rate are much larger than the DNS data. The released reaction heat can be completely converted to internal energy in the zero-dimensional model which results in a more significant increase of temperature, thus leading to a faster reactant consumption and product generation rates, according to (2.11). In contrast, in reacting turbulence simulations with exothermic reactions, a part of the internal energy will be converted to kinetic energy which results in a lower average temperature compared with zero-dimensional cases. Figure 2(*c*) shows the temporal variation of average reaction rate $\langle W\rangle$, where $W = -\dot{\omega}_A = Da\rho^2 Y_A Y_B \exp(-Ze/T)$ (Jaberi *et al.* 2000). It is shown that for isothermal reactions ($Da = 2$) at $M_t = 0.2$ and 0.8, reaction rates exhibit a rapid increase from $t = 0$ until reaching the maximum value at $t = 1$, and then exhibit a subsequent steep decrease at $t > 1$. The DNS data collapses with the zero-dimensional model result at $t > 2$. The deviation of DNS data and the zero-dimensional model result at $t < 2$ suggests that the zero-dimensional model cannot properly model the species mixing and advection process in turbulence. For exothermic reactions ($Da = 200$), the reaction rates obtained by DNS data exhibit a gradual increase reaching the maximum value at $t = 3$ and a subsequent gradual decrease. The simulated reaction rates for isothermal reactions are larger than those for exothermic reactions at $t < 4$. Figure 2(*d*) shows the temporal variation of average mixing rate $\langle G\rangle$, where mixing

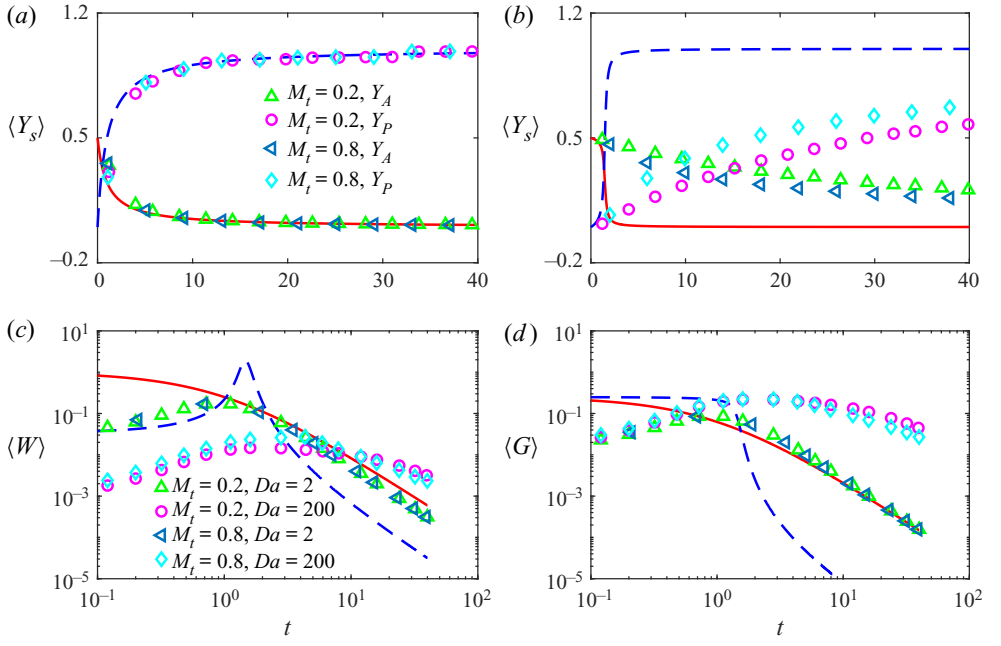

Figure 2. Temporal variation of reaction statistics for isothermal ($Da = 2$) and exothermic ($Da = 200$) reactions at turbulent Mach number $M_t = 0.2$ and 0.8 during the chemical reaction process (legend for panels (a) and (b) are identical, lines represent zero-dimensional model results): (a) average of mass fraction of species A and P for isothermal ($Da = 2$) reactions; (b) average of mass fraction of species A and P for exothermic ($Da = 200$) reactions; (c) average of reaction rate (lines represent zero-dimensional model results; solid line, W for isothermal reaction ($Da = 2$); dash line, W for exothermic reaction ($Da = 200$)); (d) average of mixing rate (lines represent zero-dimensional model results; solid line, G for isothermal reaction ($Da = 2$); dash line, G for exothermic reaction ($Da = 200$)).

rate is defined as $G = \rho^2 Y_A Y_B$ (Jaberi *et al.* 2000). It is shown that the DNS data for isothermal reaction ($Da = 2$) collapse with the zero-dimensional model result at $t > 2$. The simulated mixing rates for exothermic reactions ($Da = 200$) are larger than those for isothermal reactions ($Da = 2$) at $t > 0.6$. The above observations suggest that the zero-dimensional model can well predict the average reaction statistics for isothermal reactions beyond the initial mixing and advection phrase, and are unable to predict simulation data for exothermic reactions because of the omission of energy transfer between internal energy and kinetic energy in the zero-dimensional model.

The temporal variation of one-point statistics for isothermal ($Da = 2$) and exothermic ($Da = 200$) reactions at turbulent Mach number $M_t = 0.2$ and 0.8 during the chemical reaction process is shown in figure 3. The chemical reaction time t is normalized by large-eddy turnover time τ, where $\tau = L_I/u'$. Figures 3(a) and 3(b) show the temporal variations of the ratio of dilatational to solenoidal kinetic energy K^d/K^s and the dissipation ratio of the dilatational component to the solenoidal component of kinetic energy ϵ^d/ϵ^s at four simulation parameters. Here, the Helmholtz decomposition is applied to decompose velocity field $\boldsymbol{u}$ into a solenoidal component $\boldsymbol{u}^s$ and a dilatational component $\boldsymbol{u}^d$ (Wang *et al.* 2010): $\boldsymbol{u} = \boldsymbol{u}^s + \boldsymbol{u}^d$, where $\nabla \cdot \boldsymbol{u}^s = 0$ and $\nabla \times \boldsymbol{u}^d = 0$. The two components of kinetic energy are defined as $K^s = \langle[(u_1^s)^2 + (u_2^s)^2 + (u_3^s)^2]/2\rangle$ and $K^d = \langle[(u_1^d)^2 + (u_2^d)^2 + (u_3^d)^2]/2\rangle$. Similarly, dissipation rate of kinetic energy per unit mass is defined as $\epsilon = \epsilon^s + \epsilon^d$, where the solenoidal component is $\epsilon^s = \langle \mu/(Re\rho)\rangle\langle\omega_i\omega_i\rangle$

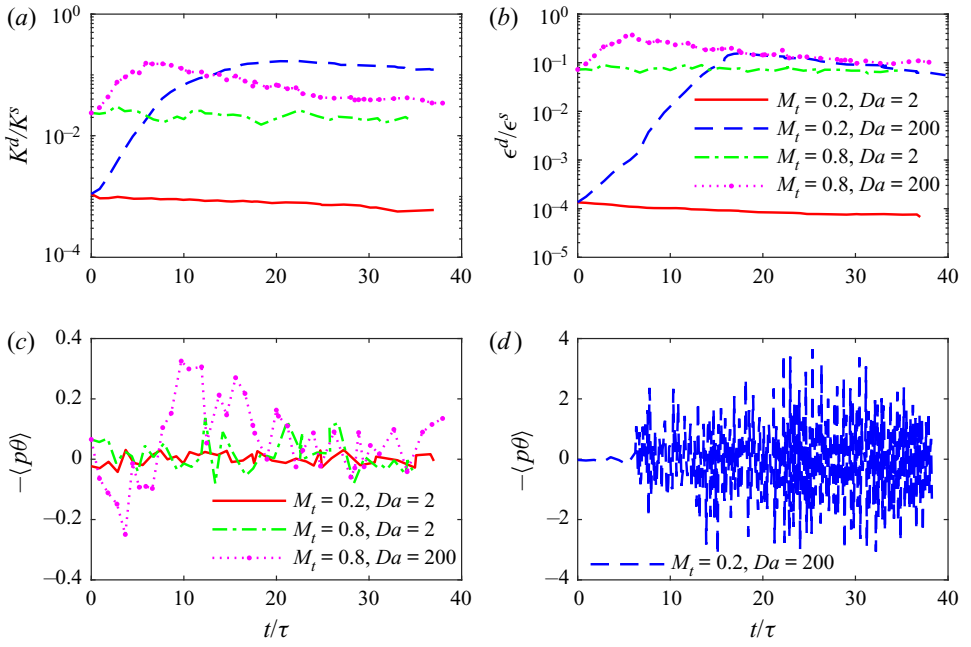

Figure 3. Temporal variation of one-point statistics for isothermal ($Da = 2$) and exothermic ($Da = 200$) reactions at turbulent Mach number $M_t = 0.2$ and 0.8 during the chemical reaction process (legend for panels (a) and (b) are identical): (a) ratio of dilatational to solenoidal kinetic energy K^d/K^s; (b) dissipation ratio of dilatational component to solenoidal component of kinetic energy ϵ^d/ϵ^s; (c) average of pressure–dilatation $-\langle p\theta\rangle$ at $M_t = 0.2$ for isothermal reaction ($Da = 2$) and at $M_t = 0.8$ for isothermal and exothermic reactions ($Da = 2$, 200); (d) average of pressure–dilatation $-\langle p\theta\rangle$ at $M_t = 0.2$ for exothermic reaction ($Da = 200$).

and the dilatational counterpart is $\epsilon^d = \langle 4\mu/(3Re\rho)\rangle\langle\theta^2\rangle$ (Samtaney *et al.* 2001; Wang *et al.* 2012*a*; Jagannathan & Donzis 2016). For isothermal reactions ($Da = 2$) at $M_t = 0.2$ and 0.8, the ratio of dilatational to solenoidal kinetic energy K^d/K^s and the dissipation ratio of dilatational component to solenoidal component of kinetic energy ϵ^d/ϵ^s remain nearly constant with a slight decrease during the entire reaction process. In contrast, for exothermic reactions ($Da = 200$) at $M_t = 0.2$ and 0.8, K^d/K^s and ϵ^d/ϵ^s increase, apparently when reactions start at $t/\tau = 0$. The increase of the dilatational part of kinetic energy can be related to the increase of energy transfer from internal energy to dilatational component of kinetic energy through pressure–dilatation work, and meanwhile the solenoidal part of the kinetic energy decreases due to an enhanced viscous dissipation (Livescu *et al.* 2002). At $t/\tau > 25$, K^d/K^s and ϵ^d/ϵ^s for all simulations reach a quasi-steady state. The temporal average of statistics in the subsequent analysis are based on simulation data at $t/\tau = 25 \sim 37$. Figures 3(c) and 3(d) show the temporal variation of average pressure–dilatation $-\langle p\theta\rangle$ for isothermal ($Da = 2$) and exothermic ($Da = 200$) reactions at turbulent Mach number $M_t = 0.2$ and 0.8 during the chemical reaction process. For isothermal reactions at $M_t = 0.2$ and 0.8 as shown in figure 3(c), $-\langle p\theta\rangle$ exhibits small fluctuations during the entire reaction process. Here 41 sampling data are used for isothermal reaction ($Da = 2$) at $M_t = 0.2$ and 0.8 and for exothermic reaction ($Da = 200$) at $M_t = 0.8$; 401 sampling data are used for exothermic reaction ($Da = 200$) at $M_t = 0.2$. For exothermic reaction ($Da = 200$) at $M_t = 0.8$, the fluctuation amplitude of $-\langle p\theta\rangle$ is slightly larger than that for isothermal reactions. For exothermic

reaction ($Da = 200$) at $M_t = 0.2$, as shown in figure 3(d), $-\langle p\theta \rangle$ exhibits large amplitude fluctuations when $t/\tau > 6$. To explain the wave-like behaviour of pressure–dilatation, Miura & Kida (1995) derived a wave equation for pressure fluctuation and concluded that the oscillation of pressure–dilatation is dominated by acoustic waves. Teng *et al.* (2020) also demonstrated that for compressible turbulence with strong heat release, the acoustic mode dominates over the dynamics of dilatational velocity and pressure.

To reveal the influence of heat release on the change of flow compressibility, figure 4 shows contours of instantaneous normalized velocity divergence θ/θ' on a slice at the end of chemical reaction $t/\tau = 35$. For isothermal reaction ($Da = 2$) at $M_t = 0.2$ as shown in figure 4(a), the contours of normalized velocity divergence exhibit large patches of compression and expansion regions. It is found that both compression and expansion motions are weak. For exothermic reaction ($Da = 200$) at $M_t = 0.2$ as shown figure 4(b), several band-like structures (blue regions, negative θ/θ') are observed, which can be identified as shocklets, where the compression is very strong. In contrast, the expansion regions (red regions, positive θ/θ') have a tendency to be blob-like and are scattered over the whole flow field. For isothermal and exothermic reactions at $M_t = 0.8$, as shown in figures 4(c) and 4(d), respectively, shocklets are also observed due to the increase of flow compressibility, and the spatial patterns of the normalized velocity divergence are similar to that observed for exothermic reaction at $M_t = 0.2$. The observations indicate that heat release through exothermic reactions can increase the flow compressibility and lead to the formation of shocklets at a low turbulent Mach number.

The isosurfaces of instantaneous normalized velocity divergence $\theta/\theta' = -2$ for isothermal ($Da = 2$) and exothermic ($Da = 200$) reactions at turbulent Mach number $M_t = 0.2$ and 0.8 at $t/\tau = 35$ are shown in figure 5. The isosurfaces are coloured by normalized heat release Q/Q'. In isothermal reactions, $Q = 0$. It is observed that for isothermal ($Da = 2$) reaction at $M_t = 0.2$, the isosurfaces of $\theta/\theta' = -2$ are small blob-like structures and are sparsely distributed. For exothermic reaction at the same turbulent Mach number, the isosurfaces of $\theta/\theta' = -2$ are significantly increased and show large sheet-like structures. Those sheet-like structures represent strong compression regions which are shocklets (Wang *et al.* 2010). Additionally, both strong and weak normalized heat release are found at strong compressive structures, which suggest that heat release is not directly related to velocity divergence. For isothermal and exothermic reactions at $M_t = 0.8$, the strong compression sheet-like structures are largely observed in the flow field. Particularly, for exothermic reaction ($Da = 200$) at $M_t = 0.8$, the negative velocity divergence regions are increased and the sheet-like structures exhibit smaller patches compared with those observed for isothermal reaction ($Da = 2$) at the same turbulent Mach number.

To obtain an intuitive visualization of species distribution in the flow field, the scalar gradient for product P is defined in terms of mass fraction (Hamlington *et al.* 2011) as follows:

$$\chi_P = \sqrt{\left(\frac{\partial Y_P}{\partial x_1}\right)^2 + \left(\frac{\partial Y_P}{\partial x_2}\right)^2 + \left(\frac{\partial Y_P}{\partial x_3}\right)^2}. \tag{3.5}$$

Figure 6 shows contours of instantaneous normalized scalar gradient $\chi_P/\langle \chi_P \rangle$ for isothermal ($Da = 2$) and exothermic ($Da = 200$) reactions at turbulent Mach number $M_t = 0.2$ and 0.8 on the same slice and at the same normalized reaction time corresponding to figure 4. For isothermal reaction at $M_t = 0.2$, as shown in figure 6(a), the randomly scattered curved lines represent a thin reaction front, in which the normalized

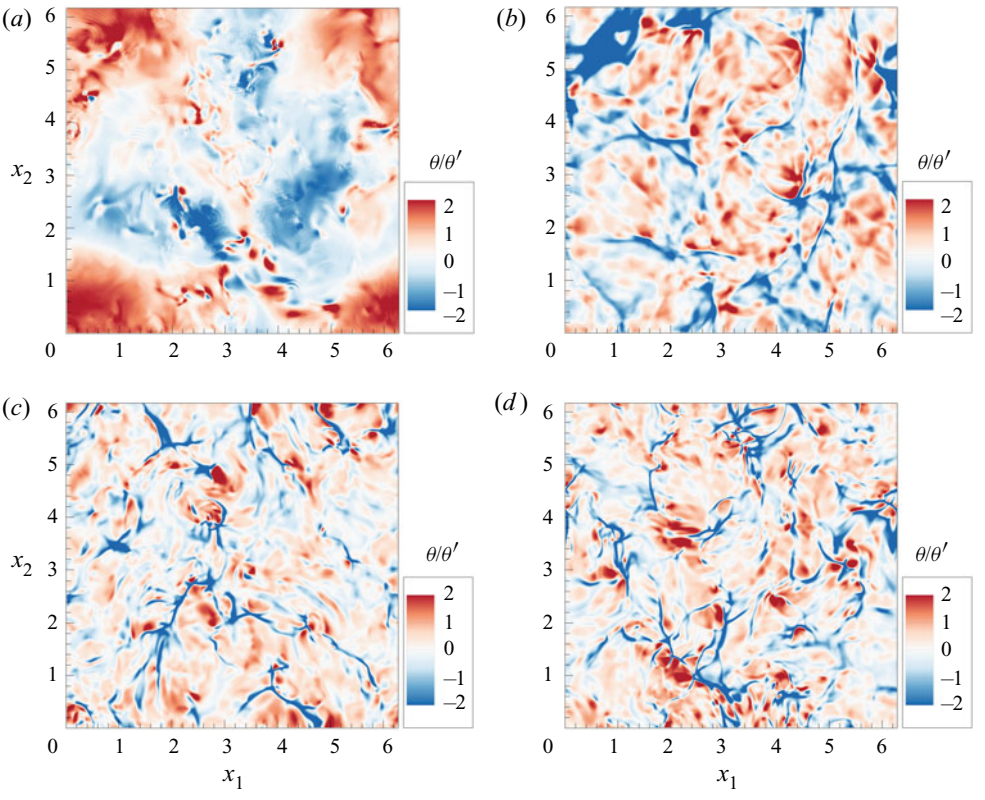

Figure 4. Contours of instantaneous normalized velocity divergence θ/θ' on a slice for isothermal ($Da = 2$) and exothermic ($Da = 200$) reactions at turbulent Mach number $M_t = 0.2$ and 0.8 at $t/\tau = 35$: (*a*) $Da = 2$, $M_t = 0.2$; (*b*) $Da = 200$, $M_t = 0.2$; (*c*) $Da = 2$, $M_t = 0.8$; and (*d*) $Da = 200$, $M_t = 0.8$.

scalar gradient $\chi_P/\langle\chi_P\rangle$ has a large value. The rest of the flow field is bounded by low values of product gradient. For exothermic reaction ($Da = 200$) at $M_t = 0.2$, as shown in figure 6(*b*), randomly distributed large scalar gradient streaks are observed. It is also observed that beside the existence of high gradient streaks, the flow field is largely occupied by scalar gradient with value $0 < \chi_P/\langle\chi_P\rangle < 2$. The contours for isothermal and exothermic reactions at $M_t = 0.8$ are similar to those for exothermic reaction at $M_t = 0.2$. The results suggest that the increase of flow compressibility at low turbulent Mach number due to strong heat release can substantially change the spatial distributions of scalar gradient and make the spatial patterns of scalar gradient similar to those at high turbulent Mach number.

It is also observed that the streak regions with large scaler gradient as shown in figures 6(*b*) and 6(*d*) are not correlated with the most compression regions as shown in figures 4(*b*) and 4(*d*). This observation can be interpreted as follows. Internal energy increased by the chemical heat release can be converted to dilatational part of kinetic energy through pressure work (Jaberi & Madnia 1998). The increased dilatational kinetic energy leads to an enhanced compression motion which consequently results in the formation of shocklets. The correlation between the product scalar gradient and velocity divergence is weak because the overall processes of energy transfer and shocklet formation are quite slow as compared with the time scale of reaction.

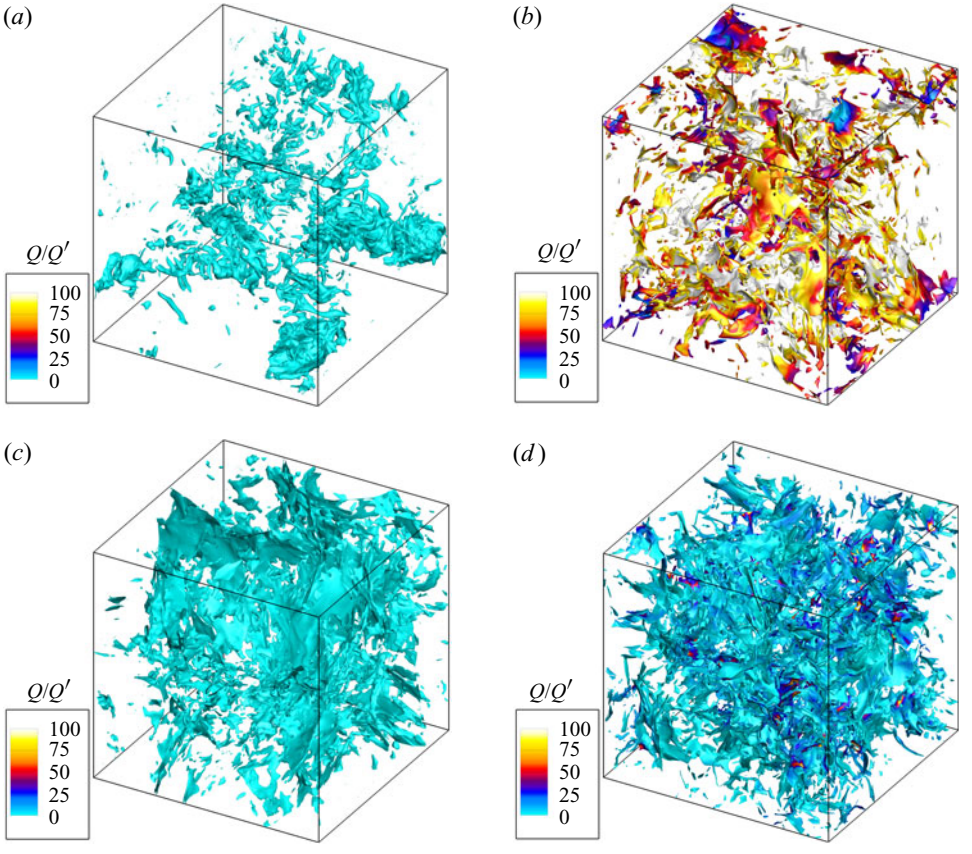

Figure 5. Isosurfaces of instantaneous normalized velocity divergence $\theta/\theta' = -2$ coloured by normalized heat release Q/Q' for isothermal ($Da = 2$) and exothermic ($Da = 200$) reactions at turbulent Mach number $M_t = 0.2$ and 0.8 at $t/\tau = 35$: (*a*) $Da = 2$, $M_t = 0.2$; (*b*) $Da = 200$, $M_t = 0.2$; (*c*) $Da = 2$, $M_t = 0.8$; and (*d*) $Da = 200$, $M_t = 0.8$.

4. Dynamical equations for filtered kinetic energy

A filtering technique (Piomelli *et al.* 1991; Martín, Piomelli & Candler 2000; Aluie 2011, 2013; Wang *et al.* 2013*a*) is utilized to analyse the interscale kinetic energy transfer in chemically reacting compressible turbulence. The filtered field $\bar{f}$ can be defined as

$$\bar{f}(\boldsymbol{x}) \equiv \int \mathrm{d}^3\, \boldsymbol{r} G_l(\boldsymbol{r}) f(\boldsymbol{x}+\boldsymbol{r}), \tag{4.1}$$

where the filter function $G_l(\boldsymbol{r}) \equiv l^{-3} G(\boldsymbol{r}/l)$, and $G(\boldsymbol{r})$ is a normalized window function. The subscript l stands for the filter width associated with the wavelength of the smallest scale retained by the filtering operation. A top-hat filter is used in subsequent analysis. In the one-dimensional calculation, it is defined as (Martín *et al.* 2000)

$$\bar{f}_i = \frac{1}{4n}\left(f_{i-n} + 2\sum_{j=i-n+1}^{i+n-1} f_j + f_{i+n} \right), \tag{4.2}$$

where the filter width is $l = 2n\Delta x$.

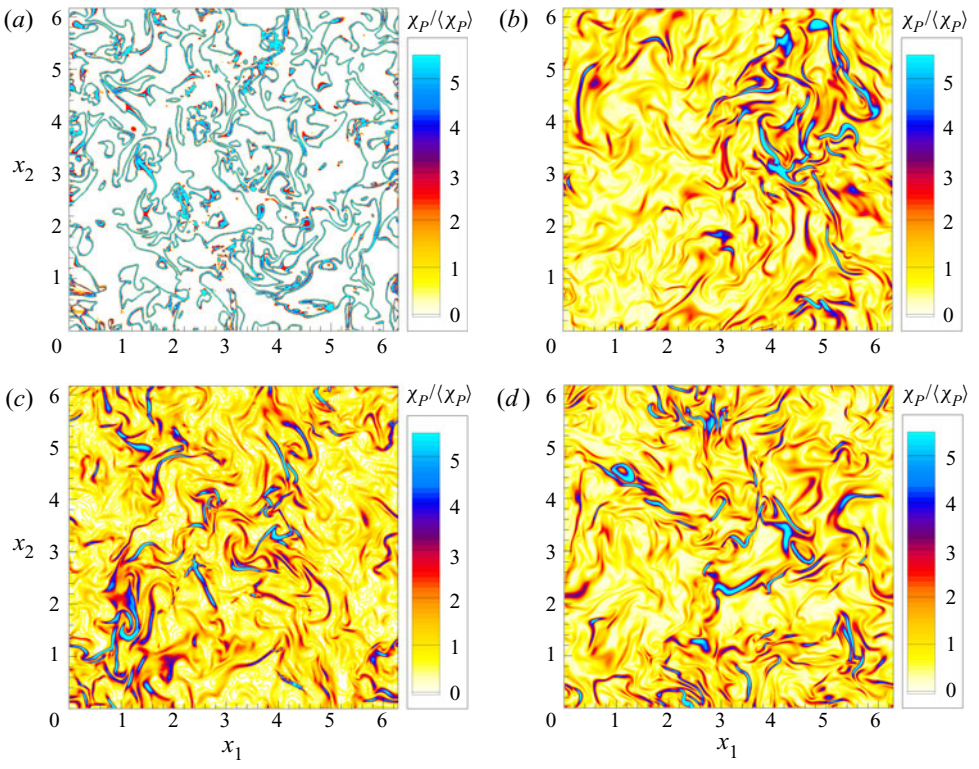

Figure 6. Contours of instantaneous normalized scalar gradient $\chi_P/\langle\chi_P\rangle$ on a slice for isothermal ($Da = 2$) and exothermic ($Da = 200$) reactions at turbulent Mach number $M_t = 0.2$ and 0.8 at $t/\tau = 35$: (*a*) $Da = 2$, $M_t = 0.2$; (*b*) $Da = 200$, $M_t = 0.2$; (*c*) $Da = 2$, $M_t = 0.8$; and (*d*) $Da = 200$, $M_t = 0.8$.

Using the Favre filtered technique $\tilde{f} \equiv \overline{\rho f}/\bar{\rho}$, the filtered equations for the density (2.1) and momentum (2.2) are expressed as (Wang *et al.* 2018*a*)

$$\frac{\partial \bar{\rho}}{\partial t} + \frac{\partial \left(\bar{\rho}\tilde{u}_j\right)}{\partial x_j} = 0, \tag{4.3}$$

$$\frac{\partial \left(\bar{\rho}\tilde{u}_i\right)}{\partial t} + \frac{\partial \left[\bar{\rho}\tilde{u}_i\tilde{u}_j + \bar{p}\delta_{ij}\right]}{\partial x_j} = -\frac{\partial \left(\bar{\rho}\tilde{\tau}_{ij}\right)}{\partial x_j} + \frac{1}{Re}\frac{\partial \bar{\sigma}_{ij}}{\partial x_j}, \tag{4.4}$$

where the SGS stress is $\bar{\rho}\tilde{\tau}_{ij} = \bar{\rho}(\widetilde{u_i u_j} - \tilde{u}_i\tilde{u}_j)$. The large-scale external forcing effect is not considered in the current analysis. The filtered equation for the large-scale kinetic energy $(1/2)\bar{\rho}\tilde{u}_i^2$ is derived as (Aluie 2011, 2013; Wang *et al.* 2013*a*, 2018*a*)

$$\frac{\partial}{\partial t}\left(\frac{1}{2}\bar{\rho}\tilde{u}_i^2\right) + J_l = -\Phi_l - \Pi_l - D_l. \tag{4.5}$$

In (4.5), J_l denotes the space transport of large-scale kinetic energy, Φ_l stands for large-scale pressure–dilatation term, Π_l represents the SGS kinetic energy flux, D_l is the

viscous dissipation term. The definition for each term is expressed as (Wang *et al.* 2018*a*)

$$J_l \equiv \frac{\partial}{\partial x_j}\left(\frac{1}{2}\bar{\rho}\tilde{u}_i^2\tilde{u}_j + \bar{p}\tilde{u}_j + \bar{\rho}\tilde{\tau}_{ij}\tilde{u}_i - \frac{\tilde{u}_i\bar{\sigma}_{ij}}{Re}\right), \tag{4.6}$$

$$\Phi_l \equiv -\bar{p}\frac{\partial \tilde{u}_i}{\partial x_i}, \tag{4.7}$$

$$\Pi_l \equiv -\bar{\rho}\tilde{\tau}_{ij}\frac{\partial \tilde{u}_i}{\partial x_j} = -\bar{\rho}\tilde{\tau}_{ij}\tilde{S}_{ij}, \tag{4.8}$$

$$D_l \equiv \frac{\bar{\sigma}_{ij}}{Re}\frac{\partial \tilde{u}_i}{\partial x_j}, \tag{4.9}$$

where, the large-scale strain tensor $\tilde{\boldsymbol{S}}$ is defined as $\tilde{S}_{ij} \equiv (1/2)(\partial\tilde{u}_i/\partial x_j + \partial\tilde{u}_j/\partial x_i)$. The average equation of the filtered kinetic energy can be expressed as

$$\frac{\partial}{\partial t}\left\langle\frac{1}{2}\bar{\rho}\tilde{u}_i^2\right\rangle = -\langle\Phi_l\rangle - \langle\Pi_l\rangle - \langle D_l\rangle\,. \tag{4.10}$$

5. Numerical results on interscale transfer of kinetic energy

Interscale transfer of kinetic energy in chemically reacting compressible isotropic turbulence is studied in this section with a focus on the effects of flow compressibility and chemical reaction over the pressure work and SGS flux of kinetic energy. The solenoidal and dilatational components of kinetic energy transfer are also investigated by Helmholtz decomposition. The statistics in the following analysis are mainly based on simulation data at $t/\tau = 25 \sim 37$. Before the discussion of interscale kinetic energy transfer, it is worthwhile to present the role of the filter width in capturing spectral information. Figure 7 shows the spectrum of the filtered velocity for isothermal ($Da = 2$) and exothermic ($Da = 200$) reactions at turbulent Mach number $M_t = 0.2$ and 0.8 for different filter widths. It can be found that with the increase of filter width, the resolved wavenumber decreases. It is also observed that the performance of filter function is nearly unaffected by turbulent Mach number and reaction heat release.

5.1. *Statistical analysis of kinetic energy transfer*

Figure 8 shows the average of energy transfer terms for isothermal ($Da = 2$) and exothermic ($Da = 200$) reactions at turbulent Mach number $M_t = 0.2$ and 0.8. The energy transfer terms are normalized by the total dissipation $\epsilon_T = -\langle p\theta\rangle + \epsilon_0$. The average of the pressure–dilatation term $\langle\Phi_l\rangle/\epsilon_T$ is plotted in figure 8(*a*). It is shown that for isothermal reactions ($Da = 2$) at $M_t = 0.2$ and 0.8, the magnitude of $\langle\Phi_l\rangle/\epsilon_T$ is negligibly small at all l/η scales. The results are consistent with the previous observations by Wang *et al.* (2018*a*) in simulating non-reacting compressible turbulence. For exothermic reaction ($Da = 200$) at $M_t = 0.2$, the magnitude of $\langle\Phi_l\rangle/\epsilon_T$ is evidently larger than that for isothermal reactions at the same turbulent Mach number for all l/η scales. At $l/\eta > 20$, the magnitude of $\langle\Phi_l\rangle/\epsilon_T$ gradually decreases with the increase of l/η. For exothermic reaction at $M_t = 0.8$, heat release results in an increase of the magnitude of $\langle\Phi_l\rangle/\epsilon_T$ at $10 \leqslant l/\eta \leqslant 100$ compared with values for isothermal reactions at the same turbulent Mach number. The results indicate that heat release through exothermic reactions can enhance the net contribution of pressure–dilatation to the kinetic energy transfer in a

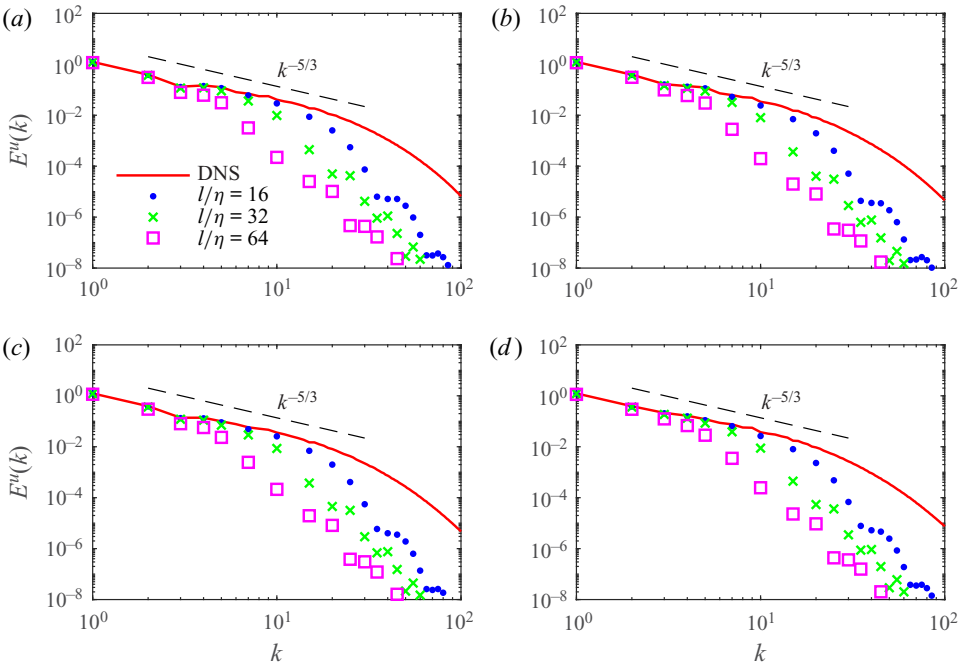

Figure 7. Spectrum of filtered velocity for isothermal ($Da = 2$) and exothermic ($Da = 200$) reactions at turbulent Mach number $M_t = 0.2$ and 0.8 for different filter widths: (*a*) $M_t = 0.2$, $Da = 2$; (*b*) $M_t = 0.2$, $Da = 200$; (*c*) $M_t = 0.8$, $Da = 2$; (*d*) $M_t = 0.8$, $Da = 200$.

wide range of scales, especially at low turbulent Mach number. Figure 8(*b*) plots the average of SGS flux $\langle \Pi_l \rangle / \epsilon_T$. It is found that $\langle \Pi_l \rangle / \epsilon_T$ nearly collapse with each other for all cases. At $2 < l/\eta < 30$, $\langle \Pi_l \rangle / \epsilon_T$ grows rapidly and at scales $30 \leqslant l/\eta \leqslant 100$, $\langle \Pi_l \rangle / \epsilon_T \approx 1.0$. For exothermic reaction at $M_t = 0.2$, $\langle \Pi_l \rangle / \epsilon_T$ is slightly larger than values for the other three cases over the entire l/η scales, indicating that heat release can enhance the relative contribution of SGS flux to kinetic energy transfer. The average of viscous dissipations $\langle D_l \rangle / \epsilon_T$ are plotted in figure 8(*c*). It is found that $\langle D_l \rangle / \epsilon_T > 0.5$ at $l/\eta \leqslant 10$, showing that viscous dissipations play an important role in kinetic energy transfer within this scale range. For all simulation cases, $\langle D_l \rangle / \epsilon_T$ decreases with the increase of filter width l/η at $l/\eta > 10$. This observation is consistent with previous theoretical analysis (Aluie 2011, 2013) and numerical results (Wang *et al.* 2018*a*) in non-reacting compressible turbulence. For exothermic reaction ($Da = 200$) at $M_t = 0.2$, $\langle D_l \rangle / \epsilon_T$ is slightly larger than values for the other three cases at all l/η scales, suggesting that strong heat release can lead to an increase of viscous dissipation. Figure 8(*d*) shows the overall energy transfer $\langle \Phi_l + \Pi_l + D_l \rangle / \epsilon_T$. It can be found that $\langle \Phi_l + \Pi_l + D_l \rangle / \epsilon_T \approx 1.0$ at scales $l/\eta \leqslant 64$ for all simulation cases and $\langle \Phi_l + \Pi_l + D_l \rangle / \epsilon_T$ is insensitive to the change of turbulent Mach number and reaction heat release. The results indicate that the effects of large-scale external forcing in current simulations are localized to large scales. In the theoretical analysis of kinetic energy transfer in compressible turbulence, Aluie (2013) proved that by using the Favre filtering for scale decomposition, the kinetic energy injection can be localized to large scales by proper stirring, such as a large-scale external acceleration field used in the current study. Results in current simulations show that heat release through

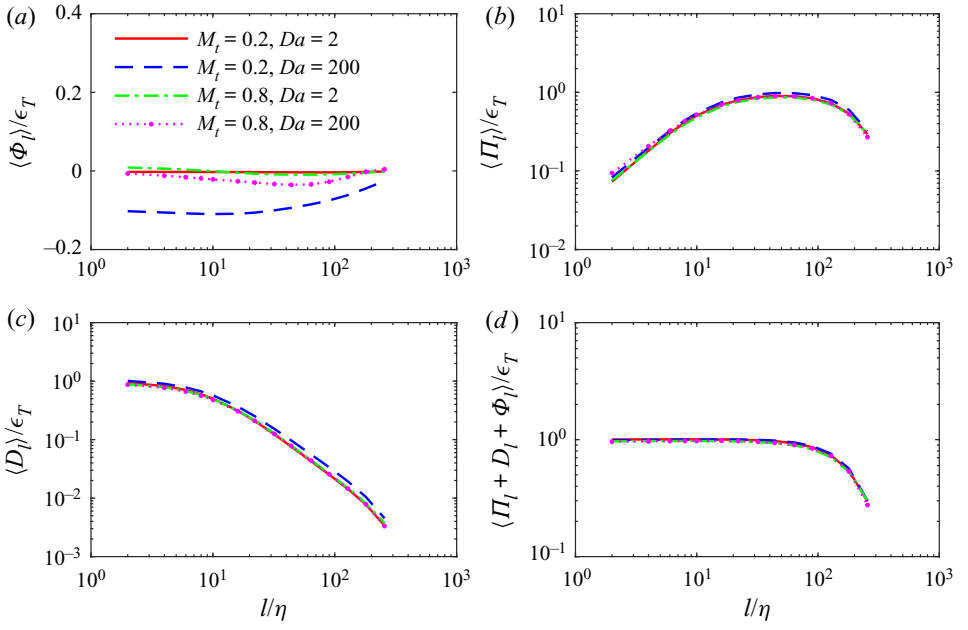

Figure 8. Average of energy transfer terms for isothermal ($Da = 2$) and exothermic ($Da = 200$) reactions at turbulent Mach number $M_t = 0.2$ and 0.8: (*a*) $\langle \Phi_l \rangle / \epsilon_T$; (*b*) $\langle \Pi_l \rangle / \epsilon_T$; (*c*) $\langle D_l \rangle / \epsilon_T$; (*d*) $\langle \Pi_l + D_l + \Phi_l \rangle / \epsilon_T$.

chemical reactions will not essentially change the behaviour of large-scale external forcing applied to the numerical system.

The normalized r.m.s. values of pressure–dilatation Φ_l'/ϵ_T and SGS flux Π_l'/ϵ_T for isothermal ($Da = 2$) and exothermic ($Da = 200$) reactions at turbulent Mach number $M_t = 0.2$ and 0.8 are shown in figure 9. Here, $\Phi_l' = \sqrt{\langle (\Phi_l - \langle \Phi_l \rangle)^2 \rangle}$ and $\Pi_l' = \sqrt{\langle (\Pi_l - \langle \Pi_l \rangle)^2 \rangle}$. As shown in figure 9(*a*), Φ_l'/ϵ_T decreases gradually with the increases of filter width l/η. For all simulation cases, $\Phi_l'/\epsilon_T > 1$ is found at all l/η scales. Particularly, for exothermic reaction ($Da = 200$) at $M_t = 0.2$, it is found that $\Phi_l'/\epsilon_T > 100$ at $l/\eta \leqslant 200$, and Φ_l'/ϵ_T is much larger than those for the other three cases at all l/η scales. Thus, the pressure–dilatation plays an important role in the local energy transfer between kinetic energy and internal energy for exothermic reactions. Heat release through exothermic reaction can significantly enhance the local transfer between kinetic energy and internal energy through pressure work, which is consistent with previous studies on chemically reacting turbulence (Jaberi & Madnia 1998; Livescu *et al.* 2002). The normalized r.m.s. value of SGS flux is shown in figure 9(*b*). It can be found that Π_l'/ϵ_T increases with the increase of filter width at $l/\eta \leqslant 20$ for all simulation cases. At a given turbulent Mach number, Π_l'/ϵ_T for exothermic reaction ($Da = 200$) is larger than that for isothermal reaction ($Da = 2$), which indicates that heat release for exothermic reactions can notably enhance the local kinetic energy transfer by SGS flux.

Figure 10 depicts the p.d.f. of the normalized pressure–dilatation Φ_l/ϵ_T for isothermal ($Da = 2$) and exothermic ($Da = 200$) reactions at turbulent Mach number $M_t = 0.2$ and 0.8. For isothermal reaction ($Da = 2$) at $M_t = 0.2$ as shown in figure 10(*a*), the p.d.f. curves of Φ_l/ϵ_T are nearly symmetric with respect to the line $\Phi_l/\epsilon_T = 0$, indicating that the compression and expansion are in a balanced state. For exothermic reaction ($Da = 200$) at $M_t = 0.2$ as shown in figure 10(*b*), both left- and right-hand tails of the p.d.f. become significantly longer than those for isothermal at the same turbulent

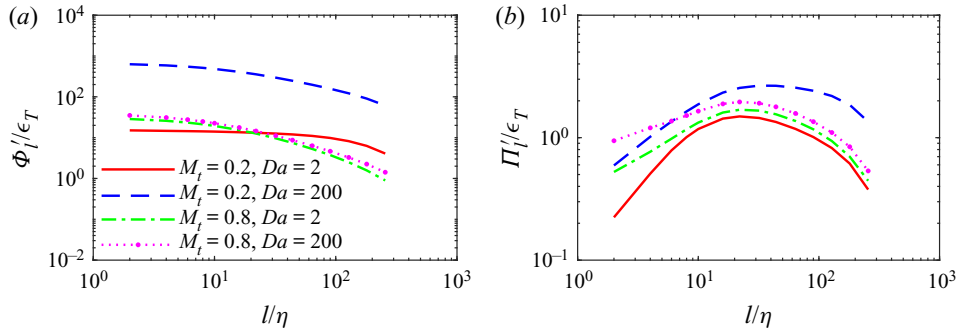

Figure 9. The r.m.s. values of pressure–dilatation and SGS flux for isothermal ($Da = 2$) and exothermic ($Da = 200$) reactions at turbulent Mach number $M_t = 0.2$ and 0.8: (*a*) Φ_l'/ϵ_T; (*b*) Π_l'/ϵ_T.

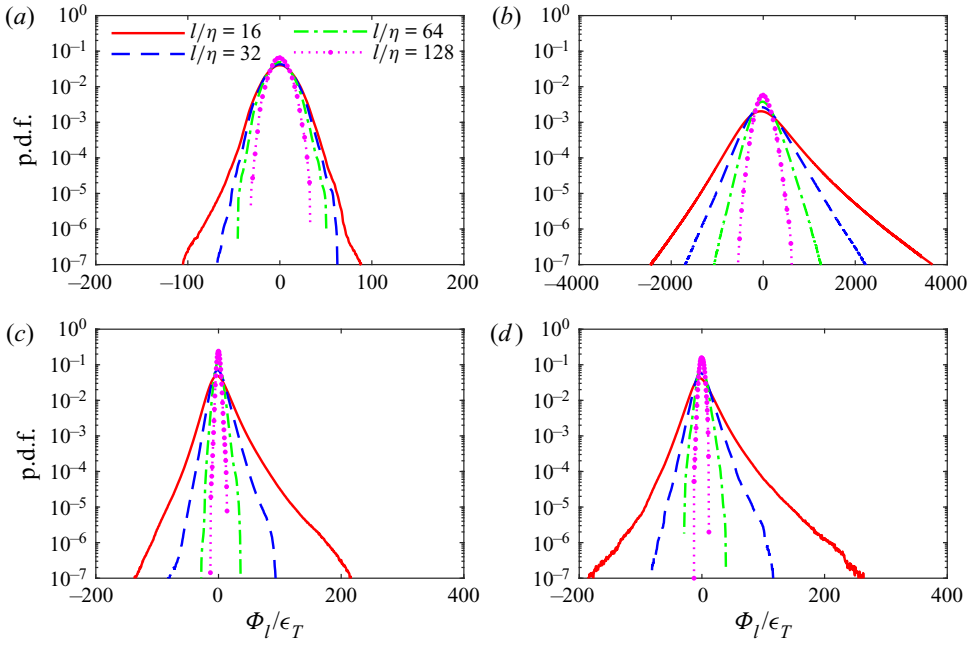

Figure 10. The p.d.f. of the normalized pressure–dilatation Φ_l/ϵ_T for isothermal ($Da = 2$) and exothermic ($Da = 200$) reactions at turbulent Mach number $M_t = 0.2$ and 0.8: (*a*) $M_t = 0.2$, $Da = 2$; (*b*) $M_t = 0.2$, $Da = 200$; (*c*) $M_t = 0.8$, $Da = 2$; (*d*) $M_t = 0.8$, $Da = 200$.

Mach number. The observation shows that heat release through exothermic reaction significantly enhances both flow compression and expansion motions. For isothermal reaction ($Da = 2$) at $M_t = 0.8$ shown in figure 10(*c*), the right-hand tail of the p.d.f. is longer than its left-hand tail, suggesting that local compression can be stronger than local expansion at high turbulent Mach number due to the increase of flow compressibility. The result is consistent with observations by Wang *et al.* (2018*a*) in simulating non-reacting compressible turbulence at high turbulent Mach numbers. For exothermic reaction ($Da = 200$) at $M_t = 0.8$ as shown in figure 10(*d*), both sides of the p.d.f. become longer. For exothermic reactions at $M_t = 0.2$ and 0.8, the right-hand tails of p.d.f. at $l/\eta = 16$ are longer than their left-hand tails, suggesting that local compression motions can be stronger than local expansion motions at small scales.

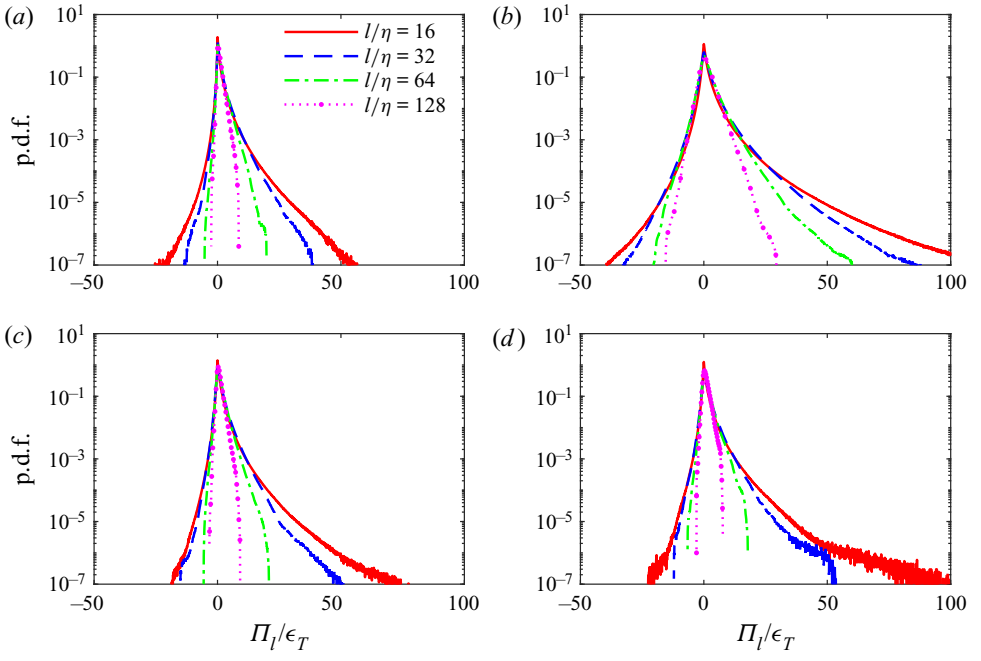

Figure 11. The p.d.f. of the normalized SGS flux Π_l/ϵ_T for isothermal ($Da = 2$) and exothermic ($Da = 200$) reactions at turbulent Mach number $M_t = 0.2$ and 0.8: (*a*) $M_t = 0.2$, $Da = 2$; (*b*) $M_t = 0.2$, $Da = 200$; (*c*) $M_t = 0.8$, $Da = 2$; (*d*) $M_t = 0.8$, $Da = 200$.

Figure 11 shows the p.d.f. of the normalized SGS flux Π_l/ϵ_T for isothermal ($Da = 2$) and exothermic ($Da = 200$) reactions at turbulent Mach number $M_t = 0.2$ and 0.8. The p.d.f. of SGS flux is skewed to the positive side, indicating that the kinetic energy transferred by SGS flux has a tendency to be from large scales to small scales. For all simulation cases, both positive and negative tails of p.d.f. become longer as the filter width l/η decreases. For isothermal reactions ($Da = 2$), with the increase of turbulent Mach number from 0.2 to 0.8 as shown in figures 11(*a*) and 11(*c*), respectively, the right-hand tails of p.d.f. of SGS flux become longer especially at small scales $l/\eta = 16$ and 32, due to the increase of flow compressibility. These observations are consistent with findings for non-reacting compressible isotropic turbulence (Wang *et al.* 2018*a*). For exothermic reactions ($Da = 200$) at $M_t = 0.2$ and 0.8, the two tails of the p.d.f. of SGS flux become longer compared with the p.d.f. for isothermal reactions ($Da = 2$) at the same turbulent Mach number. The results reveal that heat release through exothermic reactions significantly enhances local SGS energy transfer at all scales, especially at small scales. The right-hand tails of p.d.f. of SGS flux for exothermic reactions at $M_t = 0.2$ and 0.8 are longer than their left-hand tails, suggesting that the positive SGS flux is predominant over the negative SGS flux.

The pressure–dilatation Φ_l is decomposed into a positive component Φ_l^+ and a negative component Φ_l^- (O'Brien *et al.* 2014): $\Phi_l = \Phi_l^+ + \Phi_l^-$; here $\Phi_l^+ = \frac{1}{2}(\Phi_l + |\Phi_l|)$ and $\Phi_l^- = \frac{1}{2}(\Phi_l - |\Phi_l|)$. The positive pressure–dilatation indicates kinetic energy destruction by flow compression while the negative pressure–dilatation implies kinetic energy production by flow expansion (O'Brien *et al.* 2014). Figure 12 shows the normalized average of the positive and negative components of pressure–dilatation for isothermal ($Da = 2$) and exothermic ($Da = 200$) reactions at turbulent Mach number $M_t = 0.2$

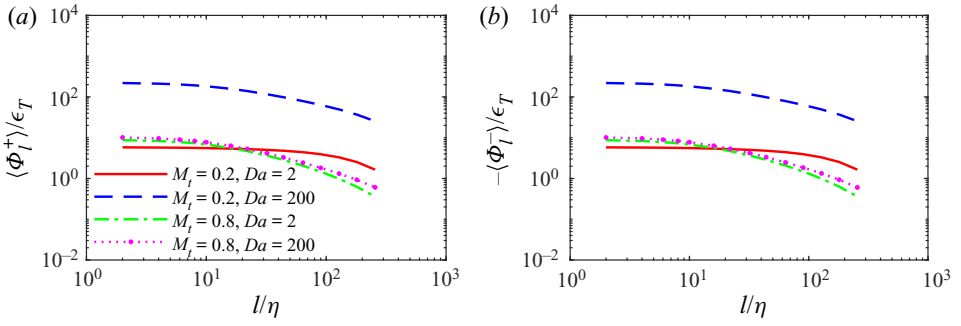

Figure 12. Normalized average of the positive and negative components of pressure–dilatation for isothermal ($Da = 2$) and exothermic ($Da = 200$) reactions at turbulent Mach number $M_t = 0.2$ and 0.8.

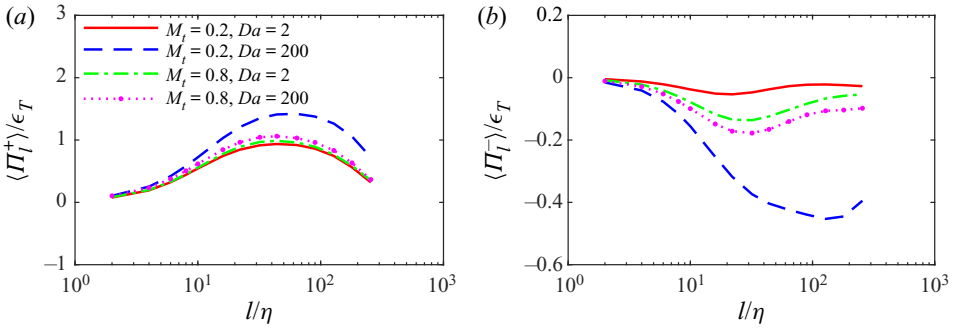

Figure 13. Normalized average of the positive and negative components of SGS flux for isothermal ($Da = 2$) and exothermic ($Da = 200$) reactions at turbulent Mach number $M_t = 0.2$ and 0.8.

and 0.8. As shown in figure 12(*a*), the positive component of pressure–dilatation for exothermic reaction ($Da = 200$) at $M_t = 0.2$ decreases gradually with the increase of filter width l/η. The magnitude of the negative component of pressure–dilatation is quite close to the positive component for all cases. For exothermic reaction ($Da = 200$) at $M_t = 0.2$, the magnitude of both positive and negative components of pressure–dilatation are significantly larger than the values for other cases at all l/η scales. The results reveal that heat release through exothermic reaction at low turbulent Mach number can significantly increase both positive and negative components of pressure–dilatation.

Similarly, the SGS flux Π_l is decomposed into a positive component Π_l^+ and a negative component Π_l^-: $\Pi_l = \Pi_l^+ + \Pi_l^-$; here $\Pi_l^+ = \frac{1}{2}(\Pi_l + |\Pi_l|)$ and $\Pi_l^- = \frac{1}{2}(\Pi_l - |\Pi_l|)$. Figure 13 shows the normalized average of the positive and negative components of SGS flux for isothermal ($Da = 2$) and exothermic ($Da = 200$) reactions at turbulent Mach number $M_t = 0.2$ and 0.8. It can be found that for isothermal reactions ($Da = 2$) at $M_t = 0.2$ and 0.8, the magnitudes of $\langle \Pi_l^+ \rangle / \epsilon_T$ and $\langle \Pi_l^- \rangle / \epsilon_T$ become larger with the increase of turbulent Mach number. At a given turbulent Mach number, the magnitudes of $\langle \Pi_l^+ \rangle / \epsilon_T$ and $\langle \Pi_l^- \rangle / \epsilon_T$ for exothermic reactions ($Da = 200$) are larger than those for isothermal reactions ($Da = 2$). Particularly, for exothermic reaction ($Da = 200$) at $M_t = 0.2$, the magnitudes of $\langle \Pi_l^+ \rangle / \epsilon_T$ and $\langle \Pi_l^- \rangle / \epsilon_T$ at $l/\eta \geqslant 20$ are significantly larger than the values for the other three cases. The magnitudes of the positive component of SGS flux are comparably larger than their negative counterparts for all cases. These observations

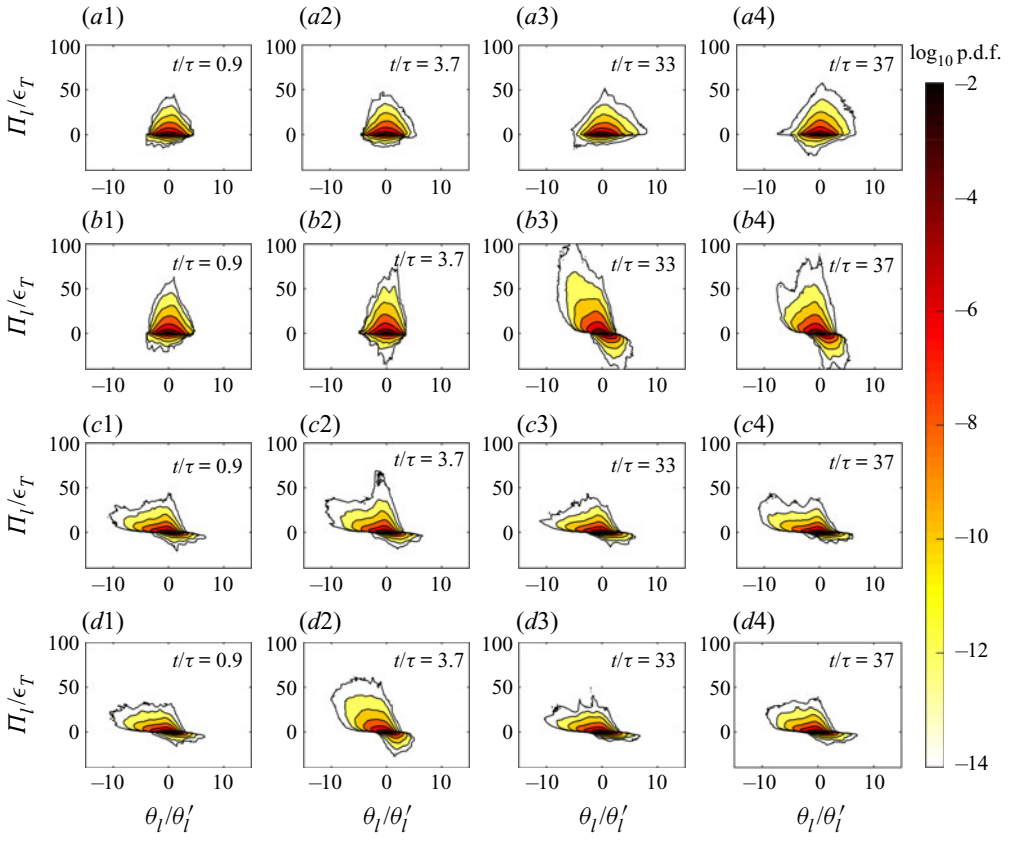

Figure 14. Joint p.d.f. of Π_l/ϵ_T and θ_l/θ_l' for the filter width $l/\eta = 16$ for isothermal ($Da = 2$) and exothermic ($Da = 200$) reactions at turbulent Mach number $M_t = 0.2$ and 0.8 at different normalized reaction time: (a1–a4) $M_t = 0.2$, $Da = 2$; (b1–b4) $M_t = 0.2$, $Da = 200$; (c1–c4) $M_t = 0.8$, $Da = 2$; (d1–d4) $M_t = 0.8$, $Da = 200$.

suggest that heat release through exothermic reactions can significantly enhance both forward-scatter and backscatter of kinetic energy through SGS flux.

5.2. *Influence of velocity divergence on SGS flux of kinetic energy*

The influences of velocity divergence on SGS flux of kinetic energy are studied in this section. Figure 14 shows the joint p.d.f. of the normalized SGS kinetic energy flux Π_l/ϵ_T and the normalized filtered velocity divergence θ_l/θ_l' with the filter width $l/\eta = 16$ for isothermal ($Da = 2$) and exothermic ($Da = 200$) reactions at turbulent Mach number $M_t = 0.2$ and 0.8 for different normalized reaction times. Here, $\theta_l = \boldsymbol{\nabla} \cdot \tilde{\boldsymbol{u}}$ is the filtered velocity divergence. Inertial-range flow quantities can exhibit some universal statistical properties and are of great importance in the study of interscale energy transfer in turbulence. The filter width performance in capturing spectral information as shown in figure 7 suggests that the filter width $l/\eta = 16$ can resolve flow quantities in the inertial-range. For isothermal reaction ($Da = 2$) at turbulent Mach number $M_t = 0.2$ as shown in figure 14(a1)–(a4), the shape of the joint p.d.f. is nearly symmetric with respect to the line $\theta_l/\theta_l' = 0$ at $t/\tau = 0.9 \sim 37$, indicating that the contributions of compression regions and expansion regions to the SGS flux are nearly equal to each other. At $t/\tau = 33$

and 37 approaching the end of chemical reaction, the positive of SGS flux is slightly enhanced corresponding to the increase of fraction of the joint p.d.f. at the positive part of Π_l in the first and second quadrants. For exothermic reaction ($Da = 200$) at $M_t = 0.2$ as shown in figure 14(b1)–(b4), the shape of the joint p.d.f. is nearly symmetric with respect to the line $\theta_l/\theta_l' = 0$ at the initial stage of the chemical reaction ($t/\tau = 0.9$). At $t/\tau = 3.7$ corresponding to the fast chemical reaction period, the fractions of the first and second quadrants of the joint p.d.f. become larger, suggesting that heat release enhances the positive SGS flux and the contributions of compression and expansion motions to the SGS flux are nearly equal to each other. At $t/\tau = 33$ and 37, the fractions of the second and fourth quadrants of the joint p.d.f. become significantly larger than those in the first and third quadrants. The joint p.d.f. for this case indicates that compression regions have a major contribution to the direct SGS flux of kinetic energy, while expansion regions have a major contribution to the reverse SGS flux of kinetic energy. The fraction of the second quadrants of the joint p.d.f. is larger than that in the forth quadrants, indicating that the occurrence of strong compression largely enhances the direct SGS flux of kinetic energy from large scales to small scales. It is worth noting that stronger compressibility is observed at $t/\tau = 33$, 37 than that at $t/\tau = 3.7$, even though heat release by the reaction is more significant at $t/\tau = 3.7$. The observation suggests that the effect of heat release on the flow compressibility is quite complicated: the internal energy increased by reaction heat can be transferred to the dilatational component of kinetic energy through pressure work, and then leads to generations of shocklets. The time scales of the overall flow dynamic processes are larger than the time scale of reaction. Consequently, the enhancement of compressibility by heat release becomes more significant after the stage of peak reaction rate. Thus, the temporal average of flow statistics based on flow fields at $t/\tau = 25 \sim 37$ can properly demonstrate the effect of heat release of reaction on the flow dynamics. For isothermal reaction ($Da = 2$) and exothermic reaction ($Da = 200$) at $M_t = 0.8$ as shown in figures 14(c1)–(c4) and 14(d1)–(d4), respectively, the joint p.d.f. exhibits similar distributions in which the p.d.f. fractions in the second and fourth quadrants are larger than those in the first and the third quadrants at $t/\tau = 0.9$. At $t/\tau = 3.7$, the fractions at second and fourth quadrants are further increased for exothermic reaction ($Da = 200$). At the end of reaction ($t/\tau = 37$), the joint p.d.f. for isothermal and exothermic reactions at $M_t = 0.8$ are similar to their initial values ($t/\tau = 0.9$). The results are consistent with observations by Wang *et al.* (2018*a*) through simulating non-reacting compressible turbulence: at $M_t > 0.6$, the second quadrant of the joint p.d.f. predominates over other three quadrants, indicating that the strong compression associated with the shocklet structures greatly enhances the direct SGS flux of kinetic energy from large scales to small scales. The influence of heat release on the joint p.d.f. through exothermic reactions is relatively less obvious at high turbulent Mach number. It should be noted that with the increase of filter width (the joint p.d.f. for $l/\eta = 32$, 64 and 128 are not plotted in the paper), the joint p.d.f. of Π_l/ϵ_T and θ_l/θ_l' becomes smaller. The qualitative statistical properties of the joint p.d.f. are nearly unaffected by the filter width.

Figure 15 plots the average of normalized SGS flux Π_l/ϵ_T conditioned on the normalized filtered velocity divergence θ_l/θ_l' with different filter widths $l/\eta = 16$, 24, 32, 48, 64 for isothermal ($Da = 2$) and exothermic ($Da = 200$) reactions at turbulent Mach number $M_t = 0.2$ and 0.8. It is shown that for isothermal reaction ($Da = 2$) at $M_t = 0.2$ as shown in figure 15(a), data are quite scattered at $\theta_l/\theta_l' \geqslant 3$ due to the lack of samples. Now $\langle \Pi_l/\epsilon_T | \theta_l/\theta_l' \rangle \approx 1$ is found at $-3 \leqslant \theta_l/\theta_l' \leqslant 3$, which indicates that the effect of local compression and expansion motions on the overall direct SGS flux of kinetic energy is negligibly small. For exothermic reaction ($Da = 200$) at $M_t = 0.2$ as

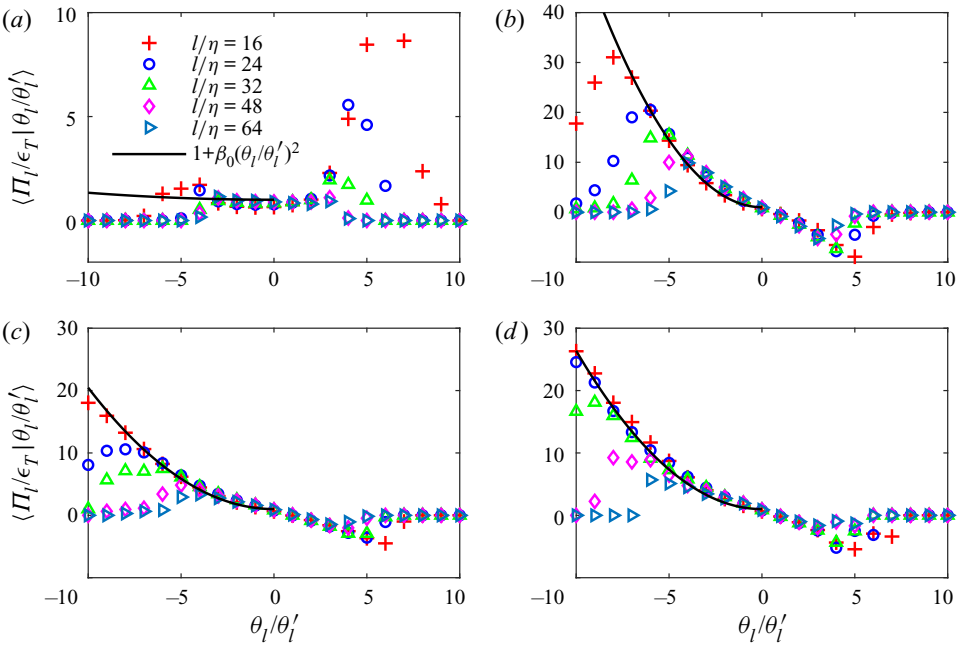

Figure 15. Average of normalized SGS flux Π_l/ϵ_T conditioned on the normalized filtered velocity divergence θ_l/θ_l' for different filter widths $l/\eta = 16$, 24, 32, 48, 64 for isothermal ($Da = 2$) and exothermic ($Da = 200$) reactions at turbulent Mach number $M_t = 0.2$ and 0.8: (*a*) $M_t = 0.2$, $Da = 2$; (*b*) $M_t = 0.2$, $Da = 200$; (*c*) $M_t = 0.8$, $Da = 2$; (*d*) $M_t = 0.8$, $Da = 200$.

shown in figure 15(*b*), data are scattered at $\theta_l/\theta_l' \leqslant -5$. The strong compression leads to strong direct SGS flux of kinetic energy, especially for small scales $l/\eta = 16$, 32. For isothermal reaction ($Da = 2$) and exothermic reaction ($Da = 200$) at $M_t = 0.8$ as shown in figures 15(*c*) and 15(*d*), respectively, the strong compression also leads to strong direct SGS flux of kinetic energy. Wang *et al.* (2018*a*) derived a heuristic model for the conditional average of SGS flux in the compression region where $\theta_l \leqslant 0$ in non-reacting compressible turbulence and observed a good agreement of the derived model with simulated data at turbulent Mach numbers $M_t = 0.6$, 0.8 and 1.0. It is reported that SGS flux of kinetic energy increases linearly with the square of filtered velocity divergence in strong compression regions. However, the derived model (Wang *et al.* 2018*a*) is no longer suitable for predicting data for reacting turbulence, especially for exothermic reactions with strong heat release. Teng *et al.* (2020) studied the Mach scaling of kinetic energy and kinetic energy dissipation in chemically reacting compressible turbulence and found that for exothermic reactions with strong heat release, the normalized kinetic energy and kinetic energy dissipation are nearly independent of turbulent Mach number. Based on the model provided by Wang *et al.* (2018*a*), a modified relation without consideration of the influence of turbulent Mach number is proposed for the conditional average of SGS flux in compression regions of chemically reacting compressible isotropic turbulence,

$$\langle \Pi_l/\epsilon_T|\theta_l/\theta_l'\rangle = 1 + \beta_0(\theta_l/\theta_l')^2, \tag{5.1}$$

where, $\beta_0 = 0.0034$ and 0.19 for isothermal reactions ($Da = 2$) at $M_t = 0.2$ and 0.8, respectively, and $\beta_0 = 0.54$ and 0.25 for exothermic reactions ($Da = 200$) at $M_t = 0.2$ and 0.8, respectively. It can be found that β_0 for exothermic reactions is larger than that for

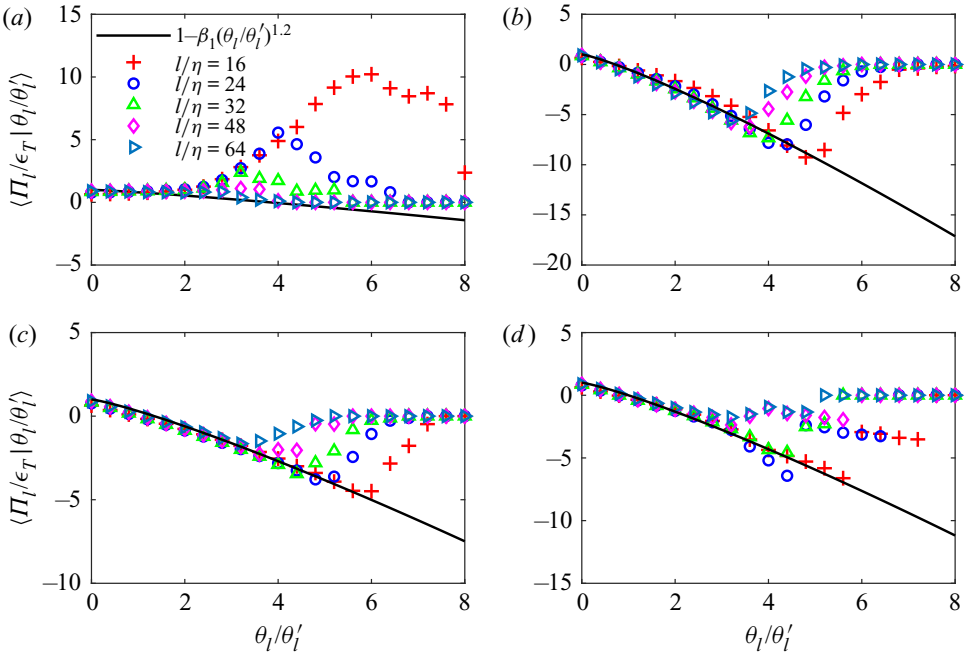

Figure 16. Average of normalized SGS flux Π_l/ϵ_T conditioned on the normalized filtered velocity divergence θ_l/θ_l' for different filter widths $l/\eta = 16$, 24, 32, 48, 64 in expansion regions for isothermal ($Da = 2$) and exothermic ($Da = 200$) reactions at turbulent Mach number $M_t = 0.2$ and 0.8: (*a*) $M_t = 0.2$, $Da = 2$; (*b*) $M_t = 0.2$, $Da = 200$; (*c*) $M_t = 0.8$, $Da = 2$; (*d*) $M_t = 0.0$, $Da = 200$.

isothermal reactions at a given turbulent Mach number, revealing the fact that heat release enhances direct SGS flux of kinetic energy at both low and high turbulent Mach numbers.

Figure 16 shows the average of normalized SGS flux Π_l/ϵ_T conditioned on the normalized filtered velocity divergence θ_l/θ_l' with different filter widths $l/\eta = 16$, 24, 32, 48, 64 in expansion regions for isothermal ($Da = 2$) and exothermic ($Da = 200$) reactions at turbulent Mach number $M_t = 0.2$ and 0.8. Based on the heuristic model proposed by Wang *et al.* (2018*a*), a modified relation in reacting compressible turbulence in expansion regions ($\theta_l \geqslant 0$) is suggested as follows:

$$\langle \Pi_l/\epsilon_T | \theta_l/\theta_l' \rangle = 1 - \beta_1 (\theta_l/\theta_l')^{1.2}. \tag{5.2}$$

As shown in figure 16, a good agreement is observed at $0 \leqslant \theta_l/\theta_l' \leqslant 5$ for all simulated cases, where, $\beta_1 = 0.2$ and 0.7 for isothermal reactions ($Da = 2$) at $M_t = 0.2$ and 0.8, respectively, and $\beta_1 = 1.50$ and 1.01 for exothermic reactions ($Da = 200$) at $M_t = 0.2$ and 0.8, respectively. It can be noticed that heat release through exothermic reactions also intensify expansion motions which result in an increase of reverse SGS flux of kinetic energy. It can also be noticed that the magnitude of conditional average of normalized SGS flux Π_l/ϵ_T in strong compression regions is much higher than that in strong expansion regions, which is consistent with a general physical insight that the flow statistics in strong compression regions are more intermittent than that in strong expansion regions for highly compressible turbulence (Wang *et al.* 2012*a*, 2017).

Figure 17 shows instantaneous isosurfaces of SGS flux coloured by normalized filtered velocity θ_l/θ_l' at $\Pi_l/\Pi_l' = 2$ with the filter width $l/\eta = 16$ for isothermal ($Da = 2$) and exothermic ($Da = 200$) reactions at turbulent Mach number $M_t = 0.2$ and 0.8 at

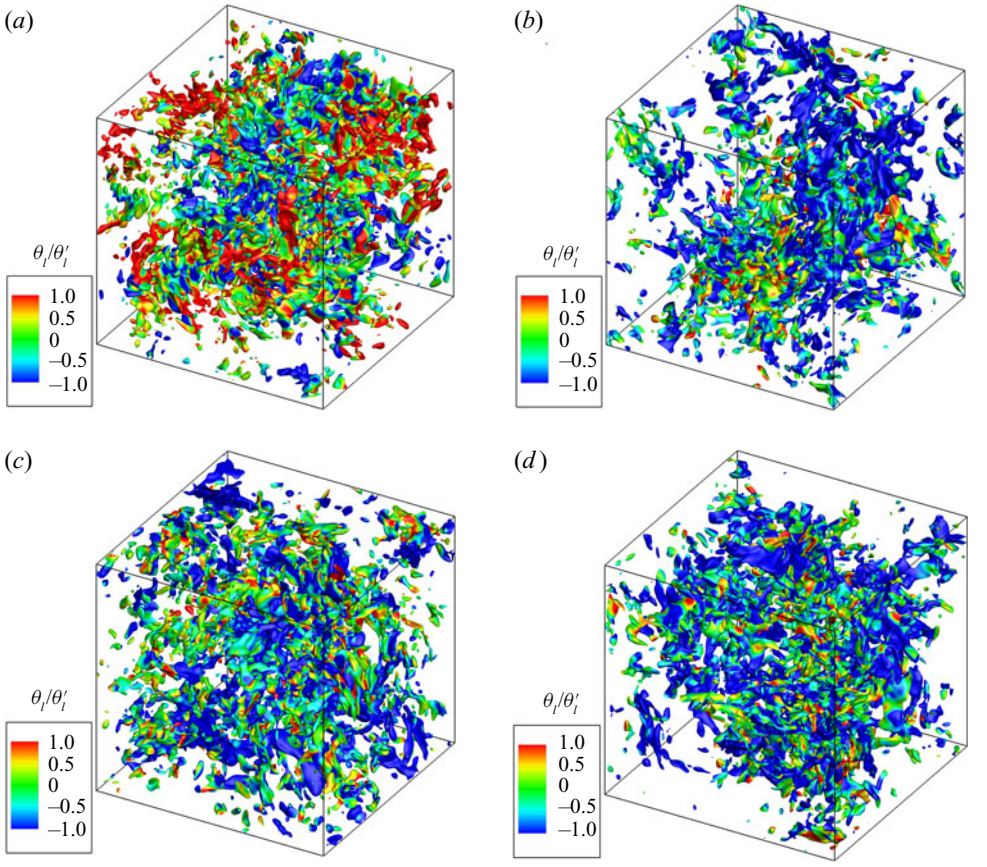

Figure 17. Isosurfaces of SGS flux coloured by normalized filtered velocity θ_l/θ_l' at $\Pi_l/\Pi_l' = 2$ for the filter width $l/\eta = 16$ for isothermal ($Da = 2$) and exothermic ($Da = 200$) reactions, at turbulent Mach number $M_t = 0.2$ and 0.8 at $t/\tau = 35$: (*a*) $M_t = 0.2$, $Da = 2$, $\Pi_l/\Pi_l' = 2$; (*b*) $M_t = 0.2$, $Da = 200$, $\Pi_l/\Pi_l' = 2$; (*c*) $M_t = 0.8$, $Da = 2$, $\Pi_l/\Pi_l' = 2$; (*d*) $M_t = 0.8$, $Da = 200$, $\Pi_l/\Pi_l' = 2$.

$t/\tau = 35$. At $M_t = 0.2$ for isothermal reaction ($Da = 2$) as shown in figure 17(*a*), the isosurfaces of $\Pi_l/\Pi_l' = 2$ can be identified as blob-like structures which are nearly uniformly distributed over the entire flow domain. Meanwhile, the fraction of compression regions and expansion regions on the isosurfaces are nearly equal to each other. For exothermic reaction ($Da = 200$) at $M_t = 0.2$ as shown in figure 17(*b*), the fraction of expansion regions are exceeded by the fraction of compression regions on the isosurfaces of $\Pi_l/\Pi_l' = 2$, which can be identified by sheet-like structures. This observation suggests that direct SGS flux of kinetic energy increases substantially due to the increase of flow compression induced by heat release at low turbulent Mach number. At $M_t = 0.8$ for isothermal ($Da = 2$) and exothermic ($Da = 200$) reactions as shown in figures 17(*c*) and 17(*d*), respectively, with the increase of flow compressibility, the fraction of sheet-like structures of $\Pi_l/\Pi_l' = 2$ increases due to the generation of shocklets, associated with strong flow compression. Heat release through exothermic reaction ($Da = 200$) promotes the formation of a larger patch of sheet-like structures of $\Pi_l/\Pi_l' = 2$ compared with the structures for the isothermal reaction situation at $M_t = 0.8$, and consequently increases the direct SGS flux of kinetic energy.

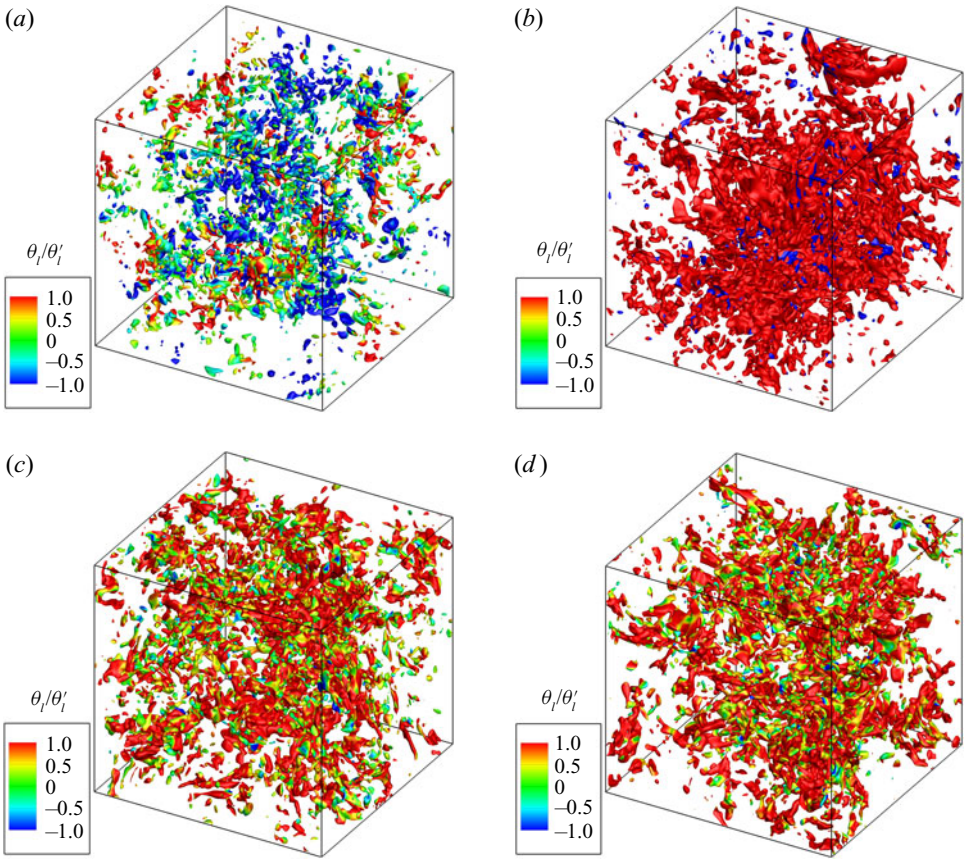

Figure 18. Isosurfaces of SGS flux coloured by normalized filtered velocity θ_l/θ_l' at $\Pi_l/\Pi_l' = -0.5$ for the filter width $l/\eta = 16$ for isothermal ($Da = 2$) and exothermic ($Da = 200$) reactions, at turbulent Mach number $M_t = 0.2$ and 0.8 at $t/\tau = 35$: (*a*) $M_t = 0.2$, $Da = 2$, $\Pi_l/\Pi_l' = -0.5$; (*b*) $M_t = 0.2$, $Da = 200$, $\Pi_l/\Pi_l' = -0.5$; (*c*) $M_t = 0.8$, $Da = 2$, $\Pi_l/\Pi_l' = -0.5$; (*d*) $M_t = 0.8$, $Da = 200$, $\Pi_l/\Pi_l' = -0.5$.

Figure 18 shows isosurfaces of SGS flux coloured by normalized filtered velocity θ_l/θ_l' at $\Pi_l/\Pi_l' = -0.5$ with the filter width $l/\eta = 16$ for isothermal ($Da = 2$) and exothermic ($Da = 200$) reactions at turbulent Mach number $M_t = 0.2$ and 0.8 at $t/\tau = 35$. At $M_t = 0.2$ for isothermal reaction ($Da = 2$) as shown in figure 18(*a*), the isosurfaces of $\Pi_l/\Pi_l' = -0.5$ can be identified as blob-like structures. However, more sparse distributions are observed compared with isosurfaces of $\Pi_l/\Pi_l' = 2$ at the same flow parameters. For exothermic reaction ($Da = 200$) at $M_t = 0.2$ as shown in figure 18(*b*), more blob-like structures associated with strong expansion regions are observed compared with isothermal reaction cases at $M_t = 0.2$. Thus, heat release induced expansion motions substantially enhance the reverse SGS flux of kinetic energy for exothermic reaction at low turbulent Mach number $M_t = 0.2$. For isothermal ($Da = 2$) and exothermic ($Da = 200$) reactions at $M_t = 0.8$ as shown in figures 18(*c*) and 18(*d*), respectively, the field is largely occupied by blob-like structures associated with strong flow expansion. Furthermore, heat release leads to minor changes of negative SGS flux structures in expansion regions at high turbulent Mach number $M_t = 0.8$.

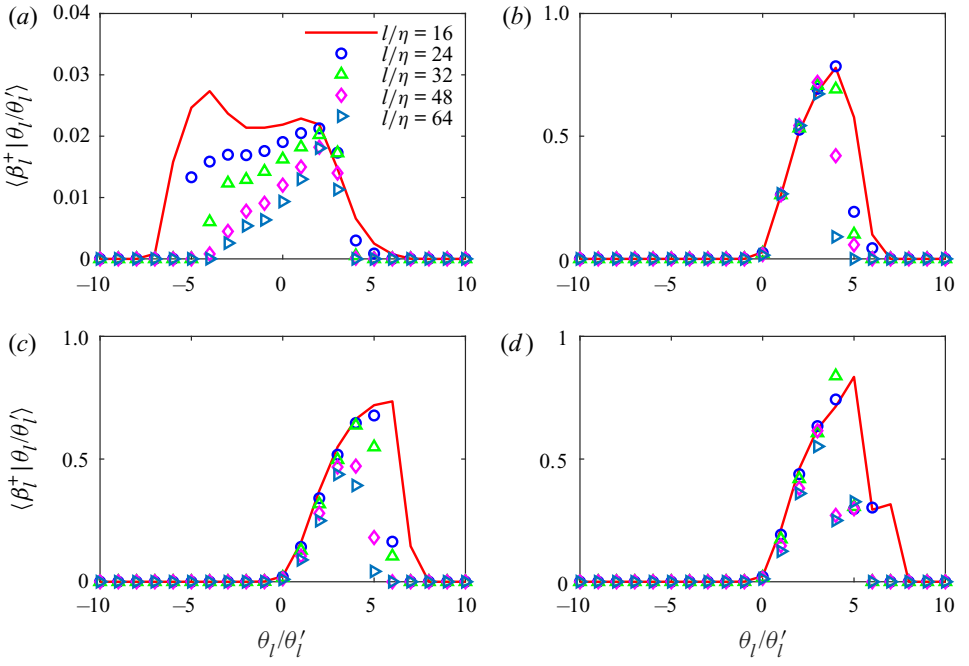

Figure 19. Average of positive β_l^+ conditioned on the normalized filtered velocity divergence θ_l/θ_l' for different filter widths $l/\eta = 16$, 24, 32, 48, 64 for isothermal ($Da = 2$) and exothermic ($Da = 200$) reactions at turbulent Mach number $M_t = 0.2$ and 0.8: (*a*) $M_t = 0.2$, $Da = 2$; (*b*) $M_t = 0.2$, $Da = 200$; (*c*) $M_t = 0.8$, $Da = 2$; (*d*) $M_t = 0.8$, $Da = 200$.

Wang *et al.* (2018*a*) defined a variable β_l to investigate the relation between the large-scale strain and the SGS stress,

$$\beta_l = \frac{\tilde{\tau}_{ij}\tilde{S}_{ij}}{|\tilde{\tau}||\tilde{\boldsymbol{S}}|}, \tag{5.3}$$

where $|\tilde{\tau}| = \sqrt{\tilde{\tau}_{ij}\tilde{\tau}_{ij}}$ and $|\tilde{\boldsymbol{S}}| = \sqrt{\tilde{S}_{ij}\tilde{S}_{ij}}$. Based on this definition, β_l is further decomposed into a positive component and a negative component: $\beta_l = \beta_l^+ + \beta_l^-$ (O'Brien *et al.* 2014), where the positive component $\beta_l^+ = \frac{1}{2}(\beta_l + |\beta_l|)$ and the negative component $\beta_l^- = \frac{1}{2}(\beta_l - |\beta_l|)$. The positive component β_l^+ indicates interscale kinetic energy backscatter and the negative component β_l^- corresponds to kinetic energy forward-scatter (Germano *et al.* 1991; Piomelli *et al.* 1991). Figures 19 and 20 show the average of two components of β_l conditioned on the normalized filtered velocity divergence θ_l/θ_l' with different filter widths $l/\eta = 16$, 24, 32, 48, 64 for isothermal ($Da = 2$) and exothermic ($Da = 200$) reactions at turbulent Mach number $M_t = 0.2$ and 0.8. For isothermal reaction ($Da = 2$) at $M_t = 0.2$ as shown in figures 19(*a*) and 20(*a*), the positive component β_l^+ and the negative component β_l^- are primarily found at $-5 \leqslant \theta_l/\theta_l' \leqslant 5$, suggesting that both flow compression and expansion contribute to the kinetic energy forward-scatter and backscatter. The magnitude for negative component β_l^- is much larger than that for the positive component β_l^+, indicating that the forward-scatter of kinetic energy is stronger than the energy backscatter. For exothermic reaction ($Da = 200$) at $M_t = 0.2$, the positive component β_l^+ is found at $0 \leqslant \theta_l/\theta_l' \leqslant 5$ (figure 19*b*) and the negative component β_l^- is

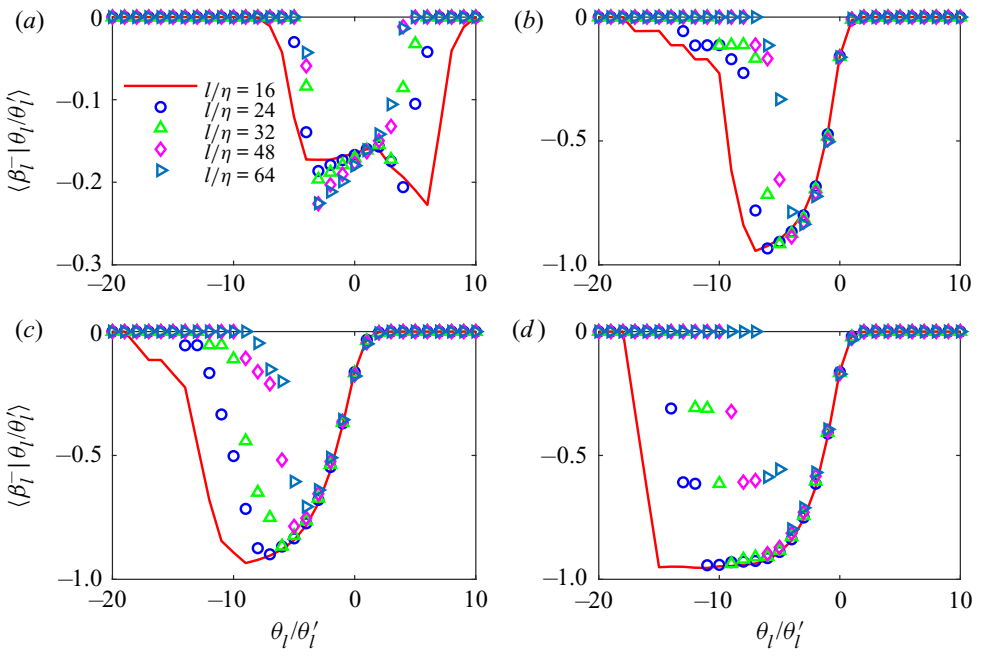

Figure 20. Average of negative β_l^- conditioned on the normalized filtered velocity divergence θ_l/θ_l' for different filter widths $l/\eta = 16, 24, 32, 48, 64$ for isothermal ($Da = 2$) and exothermic ($Da = 200$) reactions at turbulent Mach number $M_t = 0.2$ and 0.8: (*a*) $M_t = 0.2$, $Da = 2$; (*a*) $M_t = 0.2$, $Da = 200$; (*c*) $M_t = 0.8$, $Da = 2$; (*d*) $M_t = 0.8$, $Da = 200$.

found at $-10 \leqslant \theta_l/\theta_l' \leqslant 0$ (figure 20*b*). The observations reveal that flow expansion has a major contribution to the kinetic energy backscatter and the flow compression has a major contribution to the kinetic energy forward-scatter. For isothermal and exothermic reactions at $M_t = 0.8$, as shown in figures 20(*c*) and 20(*d*), respectively, the negative components $\langle \beta_l^- | \theta_l/\theta_l' \rangle$, which are close to –1, are found at $-10 \leqslant \theta_l/\theta_l' \leqslant -8$, suggesting the antiparallel alignment between the large-scale strain and the SGS stress in strong compression regions. Heat release through exothermic reactions at $M_t = 0.2$ (figure 20*b*) and 0.8 (figure 20*d*) increase the antiparallel alignment between the large-scale strain and the SGS stress.

5.3. *Helmholtz decomposition on SGS flux of kinetic energy*

Helmholtz decomposition can be applied to decompose a compressible vector field into a solenoidal part and a dilatational component. For compressible flow, the Helmholtz decomposition is applied to a density-weighted variable $\sqrt{\rho}\boldsymbol{u}$ to enforce the positive-definiteness of the spectra of the solenoidal and dilatational kinetic energies (Kida & Orszag 1990, 1992; Miura & Kida 1995; Pierre & Claude 2008; Praturi & Girimaji 2019; Donzis & John 2020). Taking the filtered density-weighted variable $\tilde{\boldsymbol{w}}$ as $\tilde{\boldsymbol{w}} = \sqrt{\rho}\tilde{\boldsymbol{u}}$, the filtered kinetic energy can be expressed as $\tilde{\boldsymbol{w}}^2/2$. Thus, the filtered equation for $\tilde{\boldsymbol{w}}$ is expressed as (Wang *et al.* 2018*a*)

$$\frac{\partial \tilde{w}_i}{\partial t} + \tilde{u}_j \frac{\partial \tilde{w}_i}{\partial x_j} + \frac{\tilde{w}_i}{2}\frac{\partial \tilde{u}_j}{\partial x_j} = -\frac{1}{\sqrt{\bar{\rho}}}\frac{\partial \bar{p}}{\partial x_i} - \frac{1}{\sqrt{\bar{\rho}}}\frac{\partial \bar{\rho}\tilde{\tau}_{ij}}{\partial x_j} + \frac{1}{\sqrt{\bar{\rho}}Re}\frac{\partial \bar{\sigma}_{ij}}{\partial x_j}. \tag{5.4}$$

Applying Helmholtz decomposition on $\tilde{\boldsymbol{w}}$ yields $\tilde{\boldsymbol{w}} = \tilde{\boldsymbol{w}}^s + \tilde{\boldsymbol{w}}^d$, where $\tilde{\boldsymbol{w}}^s$ is the solenoidal component and $\tilde{\boldsymbol{w}}^d$ is the dilatational component. The two components $\tilde{\boldsymbol{w}}^s$ and $\tilde{\boldsymbol{w}}^d$ satisfy $\boldsymbol{\nabla}\cdot\tilde{\boldsymbol{w}}^s = 0$ and $\boldsymbol{\nabla}\times\tilde{\boldsymbol{w}}^d = 0$, respectively. Multiplying (5.4) by $\tilde{w}_i^X$ yields (Wang *et al.* 2018*a*)

$$\tilde{w}_i^X\frac{\partial\tilde{w}_i}{\partial t} + \tilde{w}_i^X\left(\tilde{u}_j\frac{\partial\tilde{w}_i}{\partial x_j} + \frac{\tilde{w}_i}{2}\frac{\partial\tilde{u}_j}{\partial x_j}\right) = -\frac{\tilde{w}_i^X}{\sqrt{\bar{\rho}}}\frac{\partial\bar{p}}{\partial x_i} - \frac{\tilde{w}_i^X}{\sqrt{\bar{\rho}}}\frac{\partial\bar{\rho}\tilde{\tau}_{ij}}{\partial x_j} + \frac{\tilde{w}_i^X}{\sqrt{\bar{\rho}}Re}\frac{\partial\bar{\sigma}_{ij}}{\partial x_j}, \tag{5.5}$$

where, $X = s, d$ denotes the solenoidal component and dilatational component, respectively. The filtered equation for the average of the solenoidal (or dilatational) component of the large-scale kinetic energy is expressed as (Wang *et al.* 2018*a*)

$$\frac{\partial}{\partial t}\left\langle\frac{1}{2}\left(\tilde{w}_i^X\right)^2\right\rangle = \left\langle A_l^X\right\rangle - \left\langle\Phi_l^X\right\rangle - \left\langle\Pi_l^X\right\rangle - \left\langle D_l^X\right\rangle. \tag{5.6}$$

Here, A_l^X is the nonlinear advection term; Φ_l^X is the large-scale pressure–dilatation term; Π_l^X is the SGS kinetic energy flux; D_l^X is the viscous dissipation term. These terms are defined as (Wang *et al.* 2018*a*)

$$A_l^X \equiv -\tilde{w}_i^X\left(\tilde{u}_j\frac{\partial\tilde{w}_i}{\partial x_j} + \frac{\tilde{w}_i}{2}\frac{\partial\tilde{u}_j}{\partial x_j}\right), \tag{5.7}$$

$$\Phi_l^X \equiv -\bar{p}\frac{\partial}{\partial x_i}\left(\frac{\tilde{w}_i^X}{\sqrt{\bar{\rho}}}\right), \tag{5.8}$$

$$\Pi_l^X \equiv -\bar{\rho}\tilde{\tau}_{ij}\frac{\partial}{\partial x_j}\left(\frac{\tilde{w}_i^X}{\sqrt{\bar{\rho}}}\right), \tag{5.9}$$

$$D_l^X \equiv \frac{\bar{\sigma}_{ij}}{Re}\frac{\partial}{\partial x_j}\left(\frac{\tilde{w}_i^X}{\sqrt{\bar{\rho}}}\right). \tag{5.10}$$

It is straightforward to derive the following relations: $\langle A_l^s + A_l^d\rangle = 0$, $\Phi_l^s + \Phi_l^d = \Phi_l$, $\Pi_l^s + \Pi_l^d = \Pi_l$ and $D_l^s + D_l^d = D_l$.

Figure 21 shows the average of solenoidal and dilatational components of the nonlinear advection: $-\langle A_l^s\rangle/\epsilon_T$ and $\langle A_l^d\rangle/\epsilon_T$ for isothermal ($Da = 2$) and exothermic ($Da = 200$) reactions at turbulent Mach number $M_t = 0.2$ and 0.8. For isothermal ($Da = 2$) reaction at turbulent Mach number $M_t = 0.2$, $-\langle A_l^s\rangle/\epsilon_T$ and $\langle A_l^d\rangle/\epsilon_T$ are close to 0. For exothermic ($Da = 200$) reaction at turbulent Mach number $M_t = 0.2$, $-\langle A_l^s\rangle/\epsilon_T$ and $\langle A_l^d\rangle/\epsilon_T$ are non-negative, however, the values are also small. The results show that the kinetic energy transfer from the solenoidal mode to the dilatational mode by nonlinear advection is relatively weak for isothermal and exothermic reactions at $M_t = 0.2$. At $M_t = 0.8$ for isothermal and exothermic reactions, both $-\langle A_l^s\rangle/\epsilon_T$ and $\langle A_l^d\rangle/\epsilon_T$ decrease gradually with the increase of filter width at $10 \leqslant l/\eta \leqslant 256$, suggesting that the dilatational mode absorbs kinetic energy from the solenoidal mode at different length scales. Heat release through exothermic reaction at low and high turbulent Mach numbers exerts a small influence on the two components of the nonlinear advection.

Figure 22 shows the average of solenoidal and dilatational components of the pressure–dilatation: $\langle\Phi_l^s\rangle/\epsilon_T$ and $\langle\Phi_l^d\rangle/\epsilon_T$ for isothermal ($Da = 2$) and exothermic ($Da = 200$) reactions at turbulent Mach number $M_t = 0.2$ and 0.8. As shown in figure 22(*a*), the solenoidal component of the pressure–dilatation, $\langle\Phi_l^s\rangle/\epsilon_T$, decreases with the increase

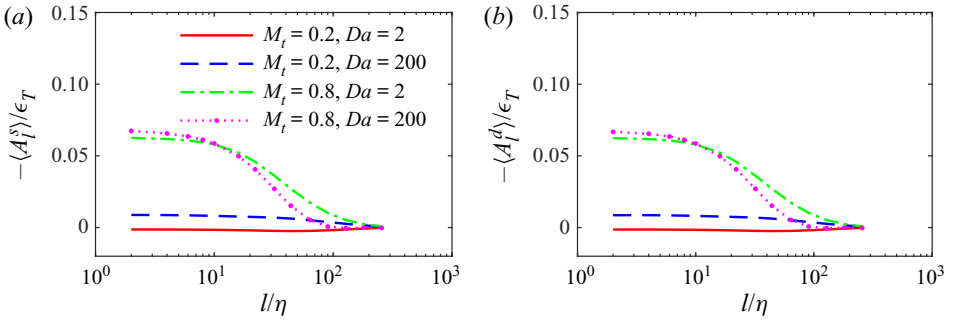

Figure 21. Average of solenoidal and dilatational components of the nonlinear advection: (*a*) $-\langle A_l^s \rangle/\epsilon_T$ and (*b*) $\langle A_l^d \rangle/\epsilon_T$.

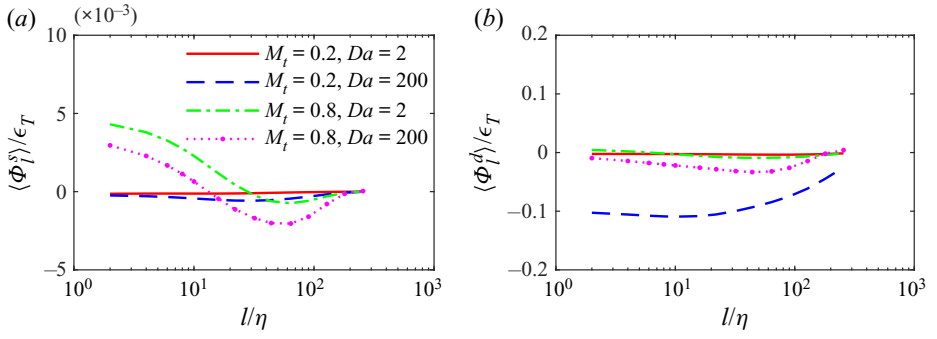

Figure 22. Average of solenoidal and dilatational components of the pressure–dilatation: (*a*) $\langle \Phi_l^s \rangle/\epsilon_T$ and (*b*) $\langle \Phi_l^d \rangle/\epsilon_T$.

of filter width l/η at $l/\eta \leqslant 60$ for isothermal and exothermic reactions at $M_t = 0.8$. The average values $\langle \Phi_l^s \rangle/\epsilon_T$ are always very small for isothermal and exothermic reactions at $M_t = 0.2$ and 0.8. The average of the dilatational component of the pressure–dilatation $\langle \Phi_l^d \rangle/\epsilon_T$ is shown in figure 22(*b*). It can be found that for isothermal reactions at $M_t = 0.2$ and 0.8, the magnitudes of dilatational component of the pressure–dilatation $\langle \Phi_l^d \rangle/\epsilon_T$ are negligibly small compared with values for exothermic reaction cases. At $M_t = 0.2$ for exothermic reaction, heat release leads to an increase of the dilatational component of the pressure–dilatation. Particularly, the magnitude of $\langle \Phi_l^d \rangle/\epsilon_T$ for exothermic reaction at $M_t = 0.2$ is significantly larger than that for exothermic reaction at $M_t = 0.8$ at all l/η scales. The magnitudes of the solenoidal component of the pressure–dilatation $\langle \Phi_l^s \rangle/\epsilon_T$ for all cases are much smaller than those of the dilatational component of the pressure–dilatation $\langle \Phi_l^d \rangle/\epsilon_T$, revealing that the dilatational component of the pressure–dilatation is much more important than the solenoidal component in kinetic energy transfer.

Figure 23 shows the average of solenoidal and dilatational components of the SGS flux: $\langle \Pi_l^s \rangle/\epsilon_T$ and $\langle \Pi_l^d \rangle/\epsilon_T$ for isothermal ($Da = 2$) and exothermic ($Da = 200$) reactions at turbulent Mach number $M_t = 0.2$ and 0.8. As shown in figure 23(*a*), the average solenoidal SGS flux $\langle \Pi_l^s \rangle/\epsilon_T$ is nearly independent of turbulent Mach number and heat release in current simulations. At $l/\eta < 30$, $\langle \Pi_l^s \rangle/\epsilon_T$ grows rapidly with the increase of filter width for all simulating cases and in the range of $30 \leqslant l/\eta \leqslant 80$, $\langle \Pi_l^s \rangle/\epsilon_T \approx 1.0$ which suggests

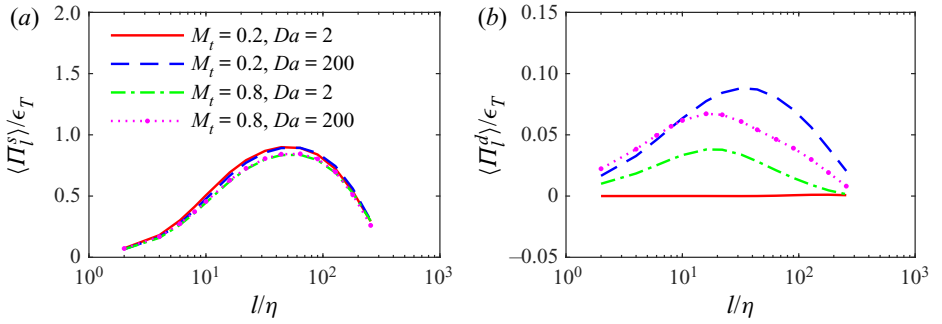

Figure 23. Average of solenoidal and dilatational components of the SGS flux: (*a*) $\langle \Pi_l^s \rangle / \epsilon_T$ and (*b*) $\langle \Pi_l^d \rangle / \epsilon_T$.

that the solenoidal component of SGS flux has a major contribution to the net transfer of kinetic energy from large scales to small scales in the range of $30 \leqslant l/\eta \leqslant 80$. In contrast, the average dilatational SGS flux $\langle \Pi_l^d \rangle / \epsilon_T$ increases evidently with the increase of turbulent Mach number for isothermal reactions ($Da = 2$) as shown in figure 23(*b*). The average dilatational SGS flux $\langle \Pi_l^d \rangle / \epsilon_T$ for exothermic reactions ($Da = 200$) are apparently larger than that for isothermal reactions ($Da = 2$) at $M_t = 0.2$ and 0.8, indicating that heat release can significantly enhance the interscale transfer of kinetic energy through the dilatational component of SGS flux. The average dilatational SGS flux $\langle \Pi_l^d \rangle / \epsilon_T$ for all cases are smaller than 0.09, implying that the contribution of dilatational component to the net flux of kinetic energy is quite small as compared with its solenoidal counterpart.

The p.d.f.s of the normalized dilatational pressure–dilatation Φ_l^d / ϵ_T for isothermal ($Da = 2$) and exothermic ($Da = 200$) reactions at turbulent Mach number $M_t = 0.2$ and 0.8 are plotted in figure 24. It is observed that for isothermal reaction ($Da = 2$) at $M_t = 0.2$ as shown in figure 24(*a*), the p.d.f.s for $16 \leqslant l/\eta \leqslant 128$ are nearly symmetric with respect to the line $\Phi_l^d / \epsilon_T = 0$, indicating that the positive part of dilatational pressure–dilatation is almost cancelled by the negative part, leading to a negligible net contribution of pressure–dilatation to the dilatational kinetic energy transfer. For isothermal reaction ($Da = 2$) at $M_t = 0.8$ as shown in figure 24(*c*), the p.d.f. at $l/\eta = 16$ is skewed toward the positive side, suggesting that the flow compression is more important than expansion in the dilatational mode of pressure–dilatation at small scales. For exothermic reactions ($Da = 200$) at $M_t = 0.2$ and 0.8, as shown in figures 24(*b*) and 24(*d*), respectively, the skewness of the p.d.f.s for both sides are increased and in addition, the right-hand tails are longer than their left-hand tails, suggesting that heat release induced flow compression plays a more important role than flow expansion in transferring dilatational kinetic energy through pressure work, especially at small scales.

Figure 25 shows that p.d.f.s of the normalized dilatational SGS flux Π_l^d / ϵ_T for isothermal ($Da = 2$) and exothermic ($Da = 200$) reactions at turbulent Mach number $M_t = 0.2$ and 0.8. For isothermal reaction ($Da = 2$) at $M_t = 0.2$ as shown in figure 25(*a*), the p.d.f.s for $16 \leqslant l/\eta \leqslant 128$ are nearly symmetric along $\Pi_l^d / \epsilon_T = 0$, indicating that the positive part of dilatational SGS flux is almost cancelled by the negative part, leading to a negligible net SGS flux of dilatational kinetic energy. At $M_t = 0.8$ for isothermal reaction ($Da = 2$) shown in figure 25(*c*), the p.d.f. is skewed toward the positive side, suggesting that the direct SGS flux of dilatational kinetic energy is larger than the reverse flux of dilatational kinetic energy. For exothermic reactions ($Da = 200$) at $M_t = 0.2$ and 0.8 shown in figures 25(*b*) and 25(*d*), respectively, the p.d.f. is skewed toward the positive

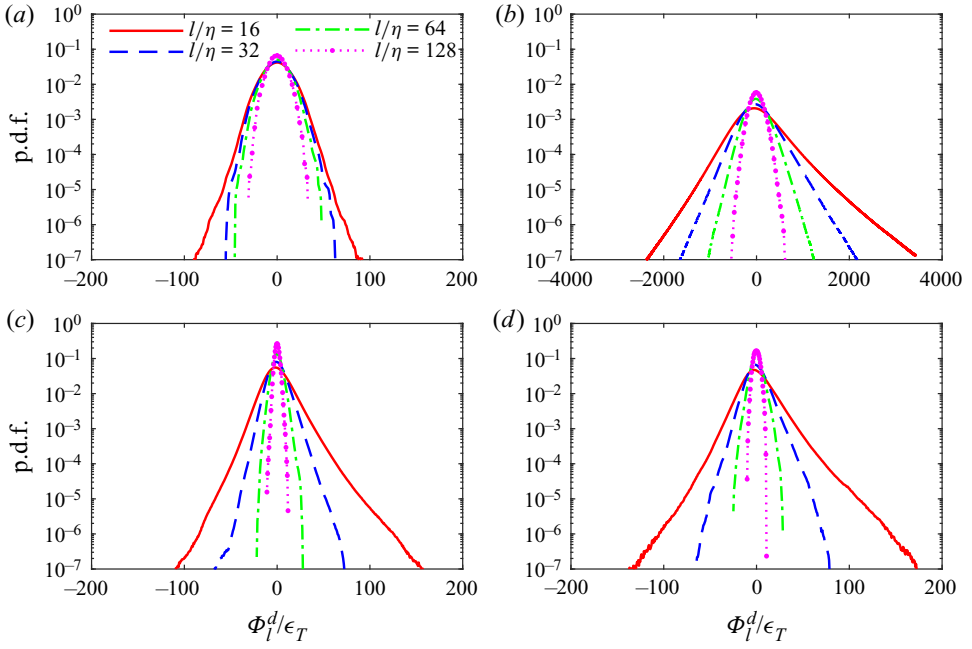

Figure 24. The p.d.f. of the normalized dilatational pressure–dilatation Φ_l^d/ϵ_T for isothermal ($Da = 2$) and exothermic ($Da = 200$) reactions at turbulent Mach number $M_t = 0.2$ and 0.8: (*a*) $M_t = 0.2$, $Da = 2$; (*b*) $M_t = 0.2$, $Da = 200$; (*c*) $M_t = 0.8$, $Da = 2$; (*d*) $M_t = 0.8$, $Da = 200$.

side, suggesting that the direct SGS flux of dilatational kinetic energy is significantly larger than the reverse flux of dilatational kinetic energy due to the effect of heat release.

Figure 26 shows the spatial–temporal average of energy transfer terms in the filtered equation of dilatational component of kinetic energy for isothermal ($Da = 2$) and exothermic ($Da = 200$) reactions at turbulent Mach number $M_t = 0.2$ and 0.8 averaged at $t/\tau = 25 \sim 37$. For isothermal reactions ($Da = 2$) at $M_t = 0.2$ and 0.8 as shown in figures 26(*a*) and 26(*c*), respectively, the average values of pressure–dilatation $-\langle\Phi_l^d\rangle/\epsilon_T$ are very small. For isothermal reaction at $M_t = 0.8$ as shown in figure 26(*c*), with the increase of flow compressibility, the nonlinear advection term $\langle A_l^d\rangle/\epsilon_T$ and the average dissipation term $-\langle D_l^d\rangle/\epsilon_T$ become more important at scales $l/\eta \leqslant 10$. The magnitudes of $\langle A_l^d\rangle/\epsilon_T$ and $-\langle D_l^d\rangle/\epsilon_T$ decay with the increase of filter width at $l/\eta > 10$. For exothermic reactions at $M_t = 0.2$ and 0.8 as shown in figures 26(*b*) and 26(*d*), respectively, the average pressure–dilatation terms $-\langle\Phi_l^d\rangle/\epsilon_T$ become important, indicating that flow compression dominates the pressure–dilatation and leads to an increase of pressure work. Heat release evidently increases the dilatational SGS flux at $10 \leqslant /\eta \leqslant 100$ and the nonlinear advection term $\langle A_l^d\rangle/\epsilon_T$ at scales $l/\eta \leqslant 10$. The overall average of dilatational components of kinetic energy transfer terms $\langle A_l^d - \Phi_l^d - \Pi_l^d - D_l^d\rangle/\epsilon_T$ for all cases are close to 0.

The average of normalized dilatational SGS flux Π_l^d/ϵ_T conditioned on the normalized filtered velocity divergence θ_l/θ_l' with different filter widths $l/\eta = 16$, 24, 32, 48, 64 for isothermal ($Da = 2$) and exothermic ($Da = 200$) reactions at turbulent Mach number $M_t = 0.2$ and 0.8 are shown in figure 27. The conditional average of dilatational SGS flux is nearly independent of filter width l/η, for $16 \leqslant l/\eta \leqslant 64$ at $-5 \leqslant \theta_l/\theta_l' \leqslant 5$ for all simulating cases. The conditional average $\langle\Pi_l^d/\epsilon_T|\theta_l/\theta_l'\rangle$ is positive in the compression

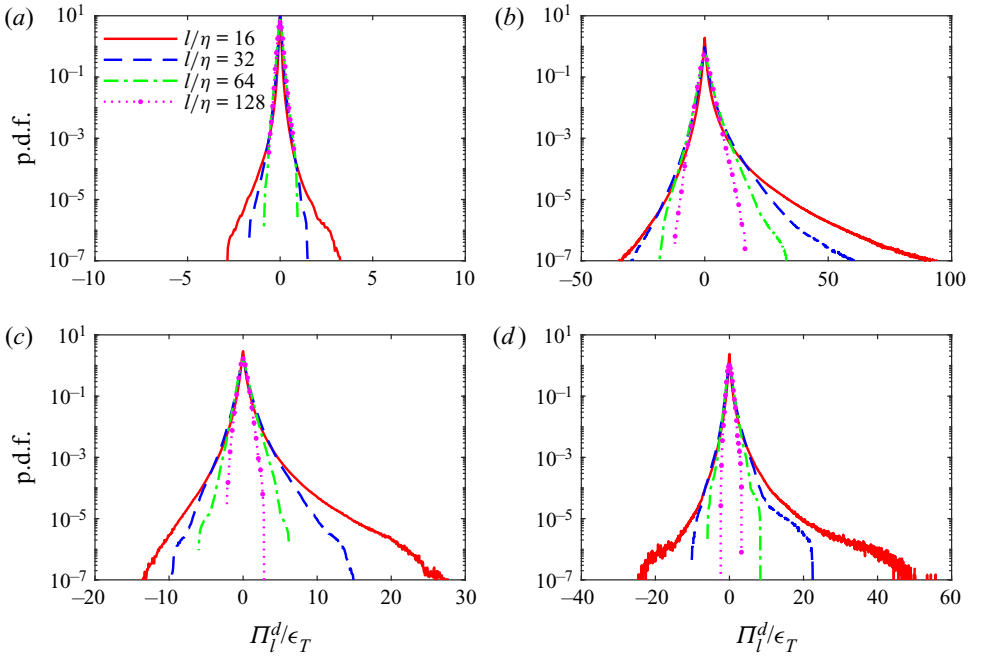

Figure 25. The p.d.f. of the normalized dilatational SGS flux Π_l^d/ϵ_T for isothermal ($Da = 2$) and exothermic ($Da = 200$) reactions at turbulent Mach number $M_t = 0.2$ and 0.8: (*a*) $M_t = 0.2$, $Da = 2$; (*b*) $M_t = 0.2$, $Da = 200$; (*c*) $M_t = 0.8$, $Da = 2$; (*d*) $M_t = 0.8$, $Da = 200$.

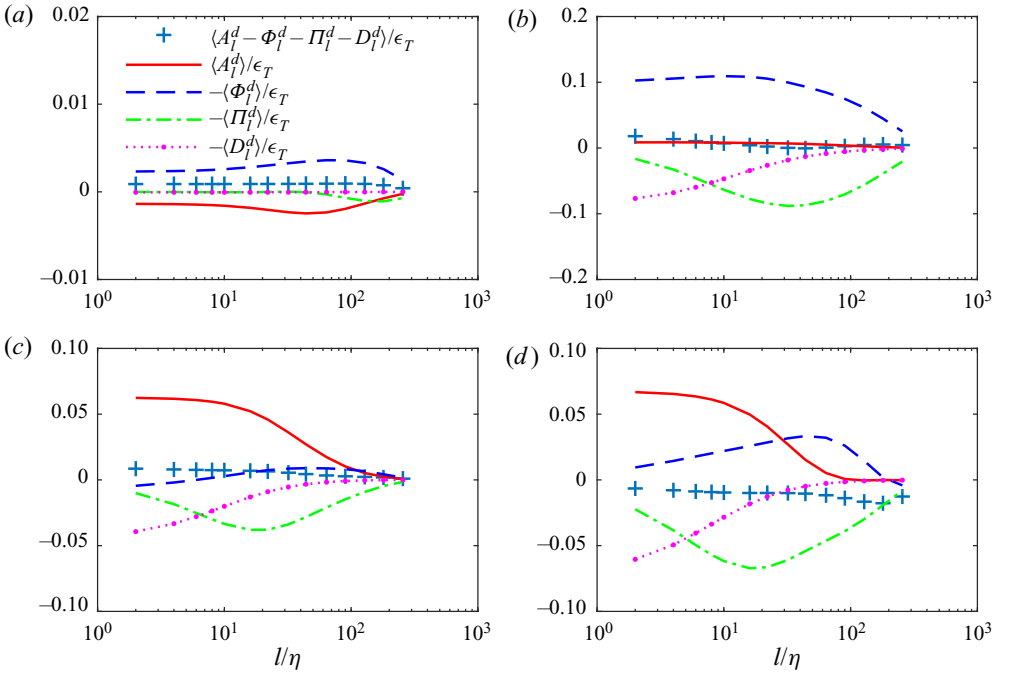

Figure 26. Average of energy transfer terms in the filtered equation of dilatational component of kinetic energy for isothermal ($Da = 2$) and exothermic ($Da = 200$) reactions at turbulent Mach number $M_t = 0.2$ and 0.8: (*a*) $M_t = 0.2$, $Da = 2$; (*b*) $M_t = 0.2$, $Da = 200$; (*c*) $M_t = 0.8$, $Da = 2$; (*d*) $M_t = 0.8$, $Da = 200$.

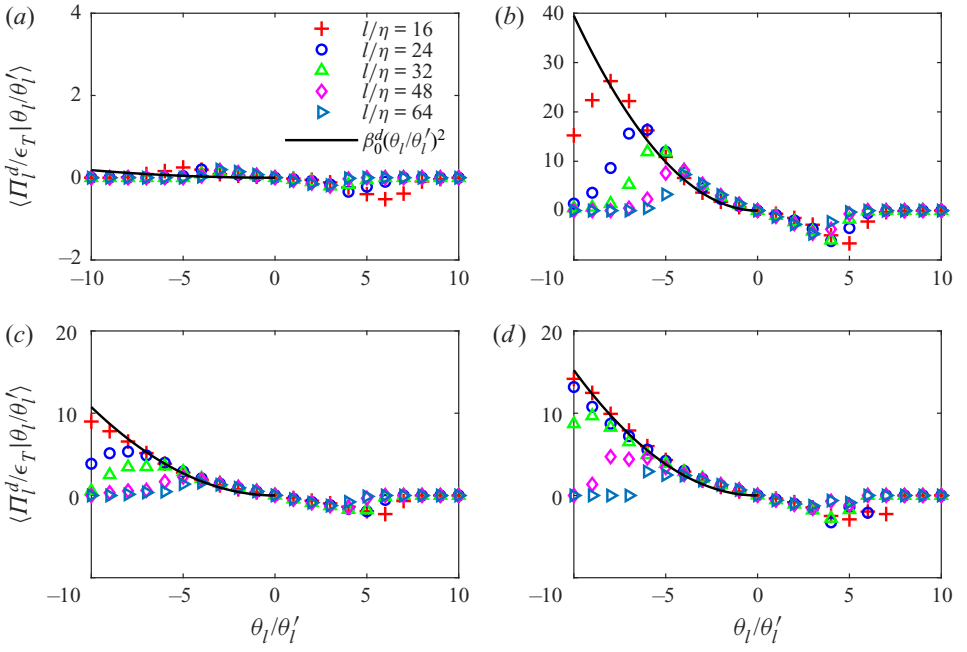

Figure 27. Average of normalized dilatational SGS flux Π_l^d/ϵ_T conditioned on the normalized filtered velocity divergence θ_l/θ_l' for different filter widths $l/\eta = 16$, 24, 32, 48, 64 for isothermal ($Da = 2$) and exothermic ($Da = 200$) reactions at turbulent Mach number $M_t = 0.2$ and 0.8: (*a*) $M_t = 0.2$, $Da = 2$; (*b*) $M_t = 0.2$, $Da = 200$; (*c*) $M_t = 0.8$, $Da = 2$; (*d*) $M_t = 0.8$, $Da = 200$.

region and is negative in the expansion region. For exothermic reactions ($Da = 200$) at $M_t = 0.2$ and 0.8 as shown in figures 27(*b*) and 27(*d*), respectively, the positive of $\langle \Pi_l^d/\epsilon_T|\theta_l/\theta_l'\rangle$ dominates over their negative counterparts, indicating that heat release enhances the direct SGS flux of dilatational kinetic energy. For non-reacting dilatational turbulence, Wang *et al.* (2018*a*) derived a simple model for the conditional average of dilatational SGS flux in the compression region $\theta_l \leqslant 0$. However, the model is no longer applicable for exothermic reactions in chemically reacting turbulence. A modified relation is proposed based on the derived model by Wang *et al.* (2018*a*),

$$\langle \Pi_l^d/\epsilon_T|\theta_l/\theta_l'\rangle = \beta_0^d(\theta_l/\theta_l')^2, \tag{5.11}$$

where, $\beta_0^d = 0.0018$ and 0.11 for isothermal reactions ($Da = 2$) at $M_t = 0.2$ and 0.8 as shown in figures 27(*a*) and 27(*c*), respectively, and $\beta_0^d = 0.39$ and 0.15 for exothermic reactions ($Da = 200$) at $M_t = 0.2$ and 0.8 as shown in figures 27(*b*) and 27(*d*), respectively. It can be found that β_0^c for exothermic reaction is larger than that for isothermal reaction at a given turbulent Mach number. Based on this relation, the average normalized solenoidal SGS flux in compression region can be derived as

$$\langle \Pi_l^s/\epsilon_T|\theta_l/\theta_l'\rangle = 1 + \beta_0^s(\theta_l/\theta_l')^2, \tag{5.12}$$

where, $\beta_0^s = \beta_0 - \beta_0^c$. Consequently, $\beta_0^s = 0.0016$ and 0.08 for isothermal reactions ($Da = 2$) at $M_t = 0.2$ and 0.8, respectively, and $\beta_0^s = 0.15$ and 0.10 for exothermic reactions ($Da = 200$) at $M_t = 0.2$ and 0.8, respectively. The coefficient β_0^s for exothermic reactions are also larger than that for isothermal reactions. The results indicate that heat release

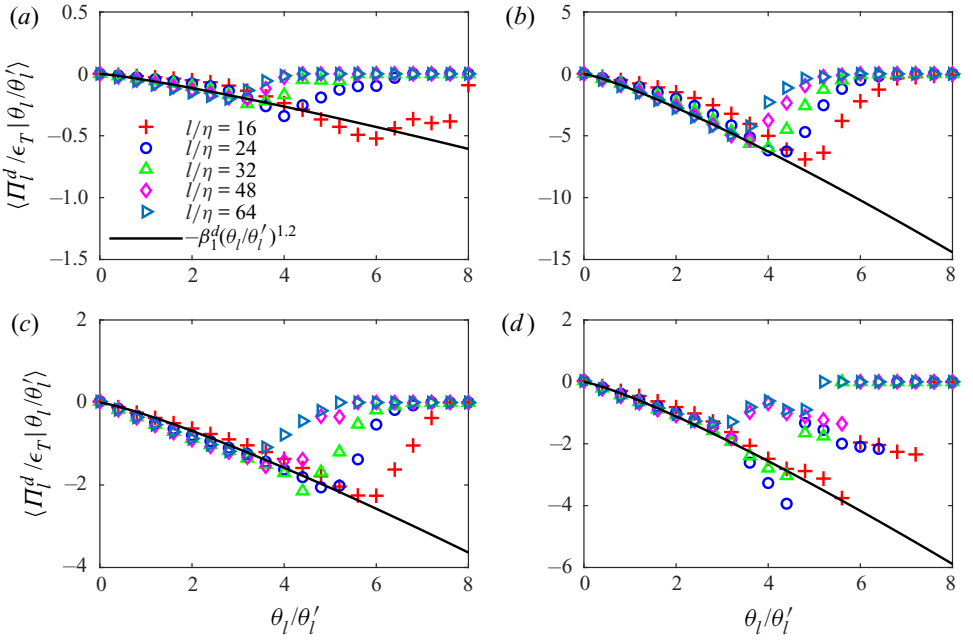

Figure 28. Average of normalized dilatational SGS flux Π_l^d/ϵ_T conditioned on the normalized filtered velocity divergence θ_l/θ_l' for different filter widths $l/\eta = 16, 24, 32, 48, 64$ in expansion regions for isothermal ($Da = 2$) and exothermic ($Da = 200$) reactions at turbulent Mach number $M_t = 0.2$ and 0.8: (*a*) $M_t = 0.2$, $Da = 2$; (*b*) $M_t = 0.2$, $Da = 200$; (*c*) $M_t = 0.8$, $Da = 2$; (*d*) $M_t = 0.8$, $Da = 200$.

enhances both dilatational SGS flux and solenoidal SGS flux of kinetic energy in compression regions.

Figure 28 shows the average of dilatational SGS flux Π_l^d/ϵ_T conditioned on the normalized filtered velocity divergence θ_l/θ_l' with different filter widths $l/\eta = 16, 24, 32, 48, 64$ in expansion regions for isothermal ($Da = 2$) and exothermic ($Da = 200$) reactions at turbulent Mach number $M_t = 0.2$ and 0.8. A modified relation based on the heuristic model derived by Wang *et al.* (2018*a*) is given for the SGS flux in expansion region of chemically reacting turbulence as

$$\langle \Pi_l^d/\epsilon_T|\theta_l/\theta_l'\rangle = -\beta_1^d(\theta_l/\theta_l')^{1.2}, \tag{5.13}$$

where, $\beta_1^d = 0.05$ and 0.30 for isothermal reactions ($Da = 2$) at $M_t = 0.2$ and 0.8 as shown in figures 28(*a*) and 28(*c*), respectively, and $\beta_1^c = 1.19$ and 0.49 for exothermic reactions ($Da = 200$) at $M_t = 0.2$ and 0.8 as shown in figures 28(*b*) and 28(*d*), respectively. Correspondingly, the average normalized solenoidal SGS flux in the expansion region can be derived as

$$\langle \Pi_l^s/\epsilon_T|\theta_l/\theta_l'\rangle = 1 - \beta_1^s(\theta_l/\theta_l')^{1.2}, \tag{5.14}$$

where, $\beta_1^s = \beta_1 - \beta_1^d$. Accordingly, $\beta_1^s = 0.15$ and 0.40 for isothermal reactions ($Da = 2$) at $M_t = 0.2$ and 0.8, respectively, and $\beta_1^s = 0.31$ and 0.52 for exothermic reactions ($Da = 200$) at $M_t = 0.2$ and 0.8, respectively, are obtained.

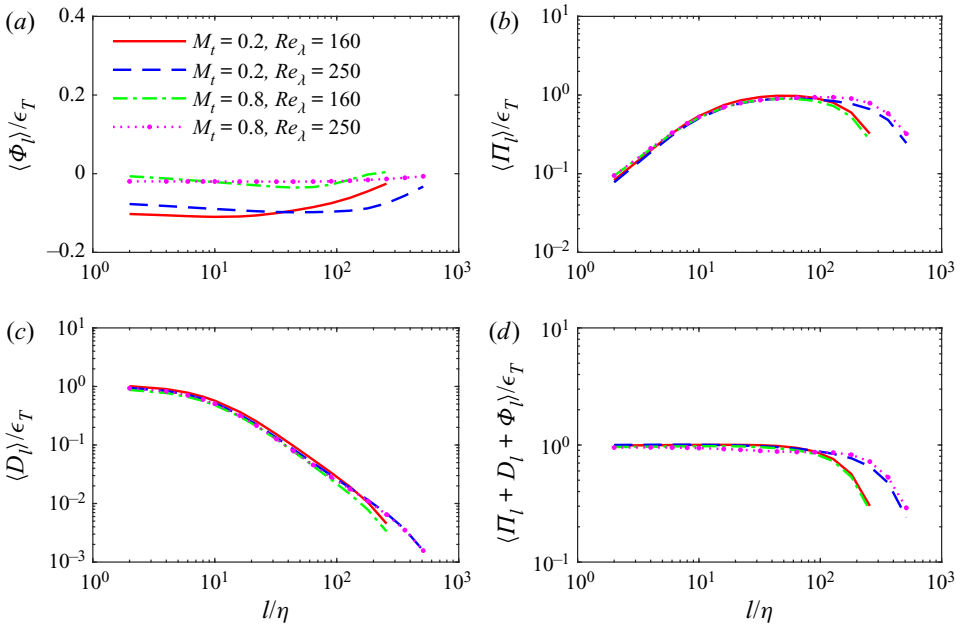

Figure 29. Average of energy transfer terms for exothermic ($Da = 200$) reactions at turbulent Mach number $M_t = 0.2$ and 0.8 and at Taylor Reynolds number $Re_\lambda \approx 160$ and 250: (*a*) $\langle \Phi_l \rangle / \epsilon_T$; (*b*) $\langle \Pi_l \rangle / \epsilon_T$; (*c*) $\langle D_l \rangle / \epsilon_T$; (*d*) $\langle \Pi_l + D_l + \Phi_l \rangle / \epsilon_T$.

6. Taylor Reynolds number effects on interscale transfer of kinetic energy

Taylor Reynolds number effects on interscale transfer of kinetic energy are analysed in this section. Through the above discussions, heat release can evidently influence interscale transfer of kinetic energy. Thus, analysis in this section is focused on exothermic reactions ($Da = 200$) at different turbulent Mach numbers and at different Taylor Reynolds numbers. Figure 29 depicts the average of energy transfer terms for exothermic ($Da = 200$) reactions at turbulent Mach number $M_t = 0.2$ and 0.8 and at Taylor Reynolds number $Re_\lambda \approx 160$ and 250. The results for Taylor Reynolds number $Re_\lambda \approx 160$ and 250 are based on DNS data solved with 512^3 and 1024^3 grids, respectively. It is observed that due to the increase of grid resolution, the average of energy transfer terms exhibit more data at large l/η values ($l/\eta > 256$) at $Re_\lambda \approx 250$ than those at $Re_\lambda \approx 160$. It is shown that the Taylor Reynolds number has a minor influence on pressure–dilatation term $\langle \Phi_l \rangle / \epsilon_T$. For the SGS flux term $\langle \Pi_l \rangle / \epsilon_T$ and viscous dissipation term $\langle D_l \rangle / \epsilon_T$, the results of two Taylor Reynolds numbers overlap each other for $l/\eta \leqslant 100$. The overall kinetic energy transfer $\langle \Pi_l + D_l + \Phi_l \rangle / \epsilon_T \approx 1.0$ at $l/\eta \leqslant 64$ for both Taylor Reynolds numbers.

The normalized average of the positive and negative components of SGS flux for exothermic ($Da = 200$) reactions at turbulent Mach number $M_t = 0.2$ and 0.8 and at Taylor Reynolds number $Re_\lambda \approx 160$ and 250 are shown in figure 30. It is observed that the magnitudes of the average of the positive and negative components of SGS flux at $M_t = 0.2$ and at $Re_\lambda \approx 250$ are slightly smaller than those at $Re_\lambda \approx 250$ at the same turbulent Mach number. The average of the positive and negative components of SGS flux at $M_t = 0.8$ are nearly unaffected by Taylor Reynolds number. The normalized average of solenoidal and dilatational components of the SGS flux for exothermic ($Da = 200$) reactions at turbulent Mach number $M_t = 0.2$ and 0.8 and at Taylor Reynolds number

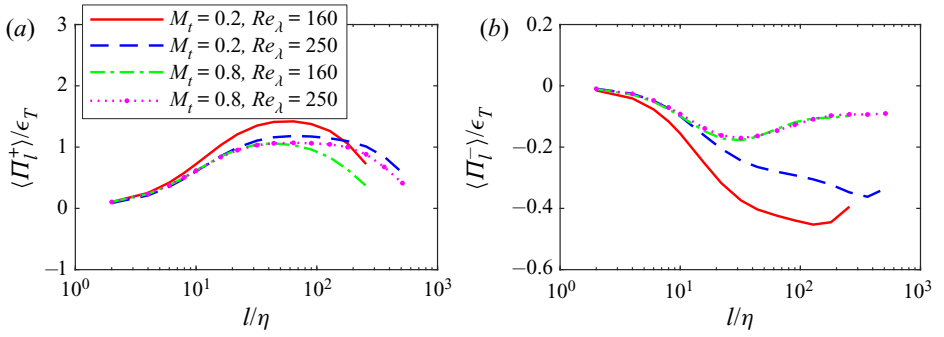

Figure 30. Normalized average of the positive and negative components of SGS flux for exothermic ($Da = 200$) reactions at turbulent Mach number $M_t = 0.2$ and 0.8 and at Taylor Reynolds number $Re_\lambda \approx 160$ and 250.

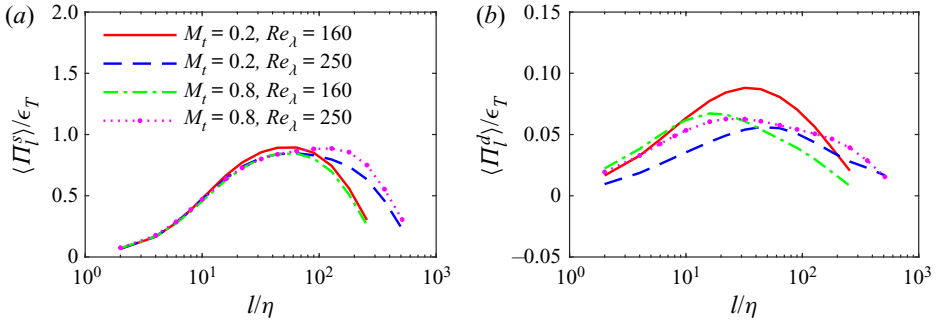

Figure 31. Normalized average of solenoidal and dilatational components of the SGS flux for exothermic ($Da = 200$) reactions at turbulent Mach number $M_t = 0.2$ and 0.8 and at Taylor Reynolds number $Re_\lambda \approx 160$ and 250: (*a*) $\langle \Pi_l^s \rangle / \epsilon_T$ and (*b*) $\langle \Pi_l^d \rangle / \epsilon_T$.

$Re_\lambda \approx 160$ and 250 are shown in figure 31. It is observed that the solenoidal components of the SGS flux collapse for $l/\eta < 100$ at $Re_\lambda \approx 160$ and 250. The dilatational components of SGS flux are slightly influenced by Taylor Reynolds number at $10 < l/\eta < 100$. The above analysis suggests that the Taylor Reynolds number has minor influence on the qualitative statistical properties of interscale kinetic energy transfer.

7. Concluding remarks

In this paper, interscale kinetic energy transfer in solenoidally forced stationary chemically reacting compressible isotropic turbulence at turbulent Mach numbers 0.2 and 0.8 is studied. Heat release of reaction enhances both compression and expansion motions. Particularly, for exothermic reaction at $M_t = 0.2$, shocklets are observed due to the intense compression motion and the spatial patterns of product gradient field are similar to those at $M_t = 0.8$ at the end of chemical reaction. The effects of heat release through exothermic reaction on flow motion and interscale kinetic energy transfer are more evident approaching the reaction end due to the time needed for reaction heat to be transferred to internal energy and then further transferred to dilatational kinetic energy, leading to the change of velocity divergence as well as SGS flux.

For exothermic reactions, the average pressure–dilatation is greatly enhanced at all l/η scales by heat release. In addition, increases of average SGS flux and average viscous

dissipation of kinetic energy are also observed. In the range of $30 \leqslant l/\eta \leqslant 200$, the average SGS flux makes a major contribution to the net transfer of filtered kinetic energy. The normalized r.m.s. values of pressure–dilatation and SGS flux are evidently increased at all l/η scales for exothermic reactions, especially at low turbulent Mach number $M_t = 0.2$. Thus, pressure work plays a more important role in local conversion between kinetic energy and internal energy for exothermic reactions. The two tails of the p.d.f.s of the normalized pressure–dilatation and normalized SGS flux for exothermic reactions are longer than those for isothermal reactions at $M_t = 0.2$ and 0.8, suggesting that heat release enhances flow compression and expansion, as well as positive and negative SGS flux.

The effect of local compressibility on the SGS kinetic energy flux is investigated. For isothermal reaction at $M_t = 0.2$, the shape of the joint p.d.f. of the SGS flux and the filtered velocity divergence is nearly symmetric with respect to the line $\theta_l/\theta_l' = 0$ throughout the entire reaction process. For isothermal reaction at $M_t = 0.8$, the joint p.d.f. primarily occupies the second and fourth quadrants due to the increase of flow compressibility. In contrast, for exothermic reaction at $M_t = 0.2$, the shape of the joint p.d.f. of the SGS flux and the filtered velocity divergence is nearly symmetric with respect to the line $\theta_l/\theta_l' = 0$ at the initial phrase of chemical reaction, then tends to expand in the first and second quadrants at the intense reaction period, and finally dominates the second and fourth quadrants. The temporal evolution of joint p.d.f. for exothermic reaction at $M_t = 0.2$ suggests that heat release induced compression motions make a major contribution to the positive SGS flux of kinetic energy, while expansion motions make a major contribution to the negative SGS flux of kinetic energy. Heat release evidently enhances the formation of negative SGS flux structures at low turbulent Mach number.

A modified relation is formulated based on the heuristic model proposed by Wang *et al.* (2018*a*) for the relation between the conditional average of SGS flux and the filtered velocity divergence, and it is found to be consistent with the numerical simulations for both isothermal and exothermic reactions. Particularly, the conditional average of SGS flux is proportional to $(\theta_l/\theta_l')^2$ in strong compression regions and $(\theta_l/\theta_l')^{1.2}$ in expansion regions. In addition, the antiparallel alignment between the large-scale strain and the SGS stress is found in strong compression regions. The study of large-scale strain and SGS flux shows that heat release can enhance the forward-scatter of kinetic energy in compression regions, and enhance the backscatter of kinetic energy in expansion regions.

Helmholtz decomposition is employed to study the interscale energy transfer of the solenoidal mode and dilatational mode. It is revealed that heat release slightly increases the solenoidal and dilatational components of nonlinear advection. The magnitude of dilatational component of pressure–dilatation increases significantly while the solenoidal component exhibits minor changes for exothermic reactions as compared with the isothermal reaction. The SGS flux of the solenoidal kinetic energy is almost unaffected by heat release, while the SGS flux of the dilatational kinetic energy is enlarged drastically by intense heat release for exothermic reactions. It is further revealed that nonlinear advection transfers the kinetic energy from the solenoidal mode to the dilatational mode. The SGS stress transfers the kinetic energy of the dilatational mode from large scales to small scales. At small scales, the viscosity irreversibly dissipates the dilatational kinetic energy into internal energy. The p.d.f.s of the normalized dilatational pressure–dilatation and normalized dilatational SGS flux are greatly increased at both left- and right-hand tails for exothermic reaction.

The interscale kinetic energy transfer for exothermic reactions at Taylor Reynolds number 160 and 250 is studied. It is shown that the overall qualitative statistical properties of kinetic energy transfer are nearly unaffected by the Taylor Reynolds number.

The magnitudes of positive and negative components of SGS flux at $Re_\lambda \approx 250$ are slightly smaller than those at $Re_\lambda \approx 160$. The solenoidal component of SGS flux is nearly unaffected by Taylor Reynolds number and the dilatational component of SGS at $Re_\lambda \approx 250$ is slightly smaller than that at $Re_\lambda \approx 160$.

In summary, a variety of effects of compressibility and heat release of chemical reaction on the pressure–dilatation and SGS flux of the kinetic energy are revealed through numerical simulations of stationary chemically reacting compressible isotropic turbulence driven by purely solenoidal forcing. The statistics and structures of pressure–dilatation and SGS flux of kinetic energy exhibit distinct features for exothermic reactions, especially at low turbulent Mach number, as compared with those for isothermal reactions. An Arrhenius type of single-step irreversible reaction is considered in this study. The effects of more realistic chemical reaction on the interscale transfer of kinetic energy in compressible turbulence remain to be further investigated.

Funding. This work was supported by National Numerical Windtunnel Project (no. NNW2019ZT1-A04), by the National Natural Science Foundation of China (NSFC grants no. 91952104, no. 11702127 and no. 91752201), by the NSFC Basic Science Center Program (grant no. 11988102), by the Technology and Innovation Commission of Shenzhen Municipality (grant nos. KQTD20180411143441009, JCYJ20170412151759222), by Key Special Project for Introduced Talents Team of Southern Marine Science and Engineering Guangdong Laboratory (Guangzhou) (grant no. GML2019ZD0103) and by Department of Science and Technology of Guangdong Province (Grant No. 2019B21203001). This work was also supported by Center for Computational Science and Engineering of Southern University of Science and Technology. J.W. acknowledges the support from Young Elite Scientist Sponsorship Program by CAST (grant no. 2016QNRC001).

Declaration of interests. The authors report no conflict of interest.

Author ORCIDs.
Jian Teng https://orcid.org/0000-0002-9088-3809;
Jianchun Wang https://orcid.org/0000-0001-5101-7791;
Hui Li https://orcid.org/0000-0002-4404-8845.

References

ALUIE, H. 2011 Compressible turbulence: the cascade and its locality. *Phys. Rev. Lett.* **106**, 174502.
ALUIE, H. 2013 Scale decomposition in compressible turbulence. *Physica* D **247** (1), 54–65.
ALUIE, H., LI, S. & LI, H. 2012 Conservative cascade of kinetic energy in compressible turbulence. *Astrophys. J.* **751** (2), L29.
BALAKRISHNAN, G., SARKAR, S. & WILLIAMS, F. 1995 Direct numerical simulation of diffusion flames with large heat release in compressible homogeneous turbulence. In *31st Joint Propulsion Conference and Exhibit*, pp. 1–15. American Institute of Aeronautics and Astronautics.
BALSARA, D.S. & SHU, C.-W. 2000 Monotonicity preserving weighted essentially non-oscillatory schemes with increasingly high order of accuracy. *J. Comput. Phys.* **160** (2), 405–452.
BARTHS, H., HASSE, C. & PETERS, N. 2000 Computational fluid dynamics modelling of non-premixed combustion in direct injection diesel engines. *Intl J. Engine Res.* **1** (3), 249–267.
CARDESA, J.I., VELA-MARTÍN, A., DONG, S. & JIMÉNEZ, J. 2015 The temporal evolution of the energy flux across scales in homogeneous turbulence. *Phys. Fluids* **27** (11), 111702.
CHEN, S. & CAO, N. 1997 Anomalous scaling and structure instability in three-dimensional passive scalar turbulence. *Phys. Rev. Lett.* **78**, 3459–3462.
CHEN, X. & LI, X. 2013 Direct numerical simulation of chemical non-equilibrium turbulent flow. *Chin. Phys. Lett.* **30** (6), 064702.
DOMARADZKI, J.A. & SAIKI, E.M. 1997 Backscatter models for large-eddy simulations. *Theor. Comput. Fluid Dyn.* **9** (2), 75–83.
DONZIS, D.A. & JOHN, J.P. 2020 Universality and scaling in homogeneous compressible turbulence. *Phys. Rev. Fluids* **5**, 084609.
DONZIS, D.A. & MAQUI, A.F. 2016 Statistically steady states of forced isotropic turbulence in thermal equilibrium and non-equilibrium. *J. Fluid Mech.* **797**, 181–200.

DUAN, L. & MARTÍN, M.P. 2011 Assessment of turbulence-chemistry interaction in hypersonic turbulent boundary layers. *AIAA J.* **49** (1), 172–184.

ESCHENROEDER, A.Q. 1964 Intensification of turbulence by chemical heat release. *Phys. Fluids* **7** (11), 1735–1743.

EYINK, G.L. & DRIVAS, T.D. 2018 Cascades and dissipative anomalies in compressible fluid turbulence. *Phys. Rev.* X **8**, 011022.

GAO, F. & OBRIEN, E.E. 1991 Direct numerical simulations of reacting flows in homogeneous turbulence. *AIChE J.* **37** (10), 1459–1470.

GERMANO, M., PIOMELLI, U., MOIN, P. & CABOT, W.H. 1991 A dynamic subgrid-scale eddy viscosity model. *Phys. Fluids* A **3** (7), 1760–1765.

GOTO, S. 2008 A physical mechanism of the energy cascade in homogeneous isotropic turbulence. *J. Fluid Mech.* **605**, 355–366.

HAMLINGTON, P.E., POLUDNENKO, A.Y. & ORAN, E.S. 2011 Interactions between turbulence and flames in premixed reacting flows. *Phys. Fluids* **23** (12), 125111.

HILL, J.C. 1976 Homogeneous turbulent mixing with chemical reaction. *Annu. Rev. Fluid Mech.* **8** (1), 135–161.

ISHIHARA, T., GOTOH, T. & KANEDA, Y. 2009 Study of high–Reynolds number isotropic turbulence by direct numerical simulation. *Annu. Rev. Fluid Mech.* **41** (1), 165–180.

JABERI, F.A. & JAMES, S. 1999 Effects of chemical reaction on two-dimensional turbulence. *J. Sci. Comput.* **14** (1), 31–72.

JABERI, F.A., LIVESCU, D. & MADNIA, C.K. 2000 Characteristics of chemically reacting compressible homogeneous turbulence. *Phys. Fluids* **12** (5), 1189–1209.

JABERI, F.A. & MADNIA, C.K. 1998 Effects of heat of reaction on homogeneous compressible turbulence. *J. Sci. Comput.* **13** (2), 201–228.

JABERI, F.A., MILLER, R.S., MADNIA, C.K. & GIVI, P. 1996 Non-Gaussian scalar statistics in homogeneous turbulence. *J. Fluid Mech.* **313** (1), 241–282.

JAGANNATHAN, S. & DONZIS, D.A. 2016 Reynolds and Mach number scaling in solenoidally-forced compressible turbulence using high-resolution direct numerical simulations. *J. Fluid Mech.* **789**, 669–707.

KIDA, S. & ORSZAG, S.A. 1990 Energy and spectral dynamics in forced compressible turbulence. *J. Sci. Comput.* **5** (2), 85–125.

KIDA, S. & ORSZAG, S.A. 1992 Energy and spectral dynamics in decaying compressible turbulence. *J. Sci. Comput.* **7** (1), 1–34.

KIM, J., BASSENNE, M., TOWERY, C.A.Z., HAMLINGTON, P.E., POLUDNENKO, A.Y. & URZAY, J. 2018 Spatially localized multi-scale energy transfer in turbulent premixed combustion. *J. Fluid Mech.* **848**, 78–116.

KNAUS, R. & PANTANO, C. 2009 On the effect of heat release in turbulence spectra of non-premixed reacting shear layers. *J. Fluid Mech.* **626**, 67–109.

KUO, K.K. & ACHARYA, R. 2012 *Applications of Turbulent and Multiphase Combustion*. Wiley.

LEE, S., LELE, S.K. & MOIN, P. 1991 Eddy shocklets in decaying compressible turbulence. *Phys. Fluids* A **3** (4), 657–664.

LEONARD, A.D. & HILL, J.C. 1992 Mixing and chemical reaction in sheared and nonsheared homogeneous turbulence. *Fluid. Dyn. Res.* **10**, 273–297.

LEONARD, A.D., HILL, J.C., MAHALINGAM, S. & FERZIGER, J.H. 1988 Analysis of homogeneous turbulent reacting flows. In *Studying Turbulence Using Numerical Simulation Databases, -II. Proc. 1988 Summer Program, Rep. CTR-S88* (ed. P. Moin, W.C. Reynolds & J. Kim), pp. 243–255. Center for Turbulence Research, Stanford University.

LESLIE, D.C. & QUARINI, G.L. 1979 The application of turbulence theory to the formulation of subgrid modelling procedures. *J. Fluid Mech.* **91** (1), 65–91.

LIBBY, P.A. & WILLIAMS, F.A. 1981 *Turbulent Reacting Flows*. Academic Press.

LIVESCU, D., JABERI, F.A. & MADNIA, C.K. 2002 The effects of heat release on the energy exchange in reacting turbulent shear flow. *J. Fluid Mech.* **450**, 35–66.

MARTÍN, M.P. & CANDLER, G.V. 1999 Subgrid-scale model for the temperature fluctuations in reacting hypersonic turbulent flows. *Phys. Fluids* **11** (9), 2765–2771.

MARTÍN, M.P., PIOMELLI, U. & CANDLER, G. 2000 Subgrid-scale models for compressible large-eddy simulations. *Theor. Comput. Fluid Dyn.* **13** (5), 361–376.

MIURA, H. & KIDA, S. 1995 Acoustic energy exchange in compressible turbulence. *Phys. Fluids* **7** (7), 1732–1742.

O'BRIEN, J., TOWERY, C.A.Z., HAMLINGTON, P.E., IHME, M., POLUDNENKO, A.Y. & URZAY, J. 2017 The cross-scale physical-space transfer of kinetic energy in turbulent premixed flames. *Proc. Combust. Inst.* **36** (2), 1967–1975.

O'Brien, J., Urzay, J., Ihme, M., Moin, P. & Saghafian, A. 2014 Subgrid-scale backscatter in reacting and inert supersonic hydrogen–air turbulent mixing layers. *J. Fluid Mech.* **743**, 554–584.

Paes, P. & Xuan, Y. 2018 Numerical investigation of turbulent kinetic energy dynamics in chemically-reacting homogeneous turbulence. *Flow Turbul. Combust.* **101** (3), 1–20.

Peters, N. 2000 *Turbulent Combustion.* Cambridge Monographs on Mechanics, vol. 1. Cambridge University Press.

Pierre, S. & Claude, C. 2008 *Homogeneous Turbulence Dynamics*. Cambridge University Press.

Piomelli, U., Cabot, W.H., Moin, P. & Lee, S. 1991 Subgrid-scale backscatter in turbulent and transitional flows. *Phys. Fluids* A **3** (7), 1766–1771.

Pope, S.B. 2000 *Turbulent Flows*. Cambridge University Press.

Praturi, D.S. & Girimaji, S.S. 2019 Effect of pressure–dilatation on energy spectrum evolution in compressible turbulence. *Phys. Fluids* **31** (5), 055114.

Richardson, L.F. & Lynch, P. 2007 *Weather Prediction by Numerical Process*. Cambridge University Press.

Sagaut, P. & Cambon, C. 2008 *Compressible Homogeneous Isotropic Turbulence*, pp. 273–326. Cambridge University Press.

Samtaney, R., Pullin, D.I. & Kosović, B. 2001 Direct numerical simulation of decaying compressible turbulence and shocklet statistics. *Phys. Fluids* **13** (5), 1415–1430.

Teng, J., Wang, J., Li, H. & Chen, S. 2020 Spectra and scaling in chemically reacting compressible isotropic turbulence. *Phys. Rev. Fluids* **5**, 084601.

Towery, C., Poludnenko, A., Urzay, J., Obrien, J., Ihme, M. & Hamlington, P.E. 2016 Spectral kinetic energy transfer in turbulent premixed reacting flows. *Phys. Rev.* E **93** (5), 053115.

Urzay, J., Ihme, M., Moin, P. & Saghafian, A. 2013 Backscatter of turbulent kinetic energy in chemically-reacting compressible flows. In *Annual Research Briefs*, pp. 123–139. Stanford University, sourced from Microsoft Academic, https://academic.microsoft.com/paper/2550236248.

Wang, J., Gotoh, T. & Watanabe, T. 2017 Spectra and statistics in compressible isotropic turbulence. *Phys. Rev. Fluids* **2** (1), 013403.

Wang, J., Shi, Y., Wang, L., Xiao, Z., He, X.T. & Chen, S. 2011 Effect of shocklets on the velocity gradients in highly compressible isotropic turbulence. *Phys. Fluids* **23** (12), 125103.

Wang, J., Shi, Y., Wang, L., Xiao, Z., He, X.T. & Chen, S. 2012*a* Effect of compressibility on the small-scale structures in isotropic turbulence. *J. Fluid Mech.* **713**, 588–631.

Wang, J., Shi, Y., Wang, L.-P., Xiao, Z., He, X.T. & Chen, S. 2012*b* Scaling and statistics in three-dimensional compressible turbulence. *Phys. Rev. Lett.* **108**, 214505.

Wang, J., Wan, M., Chen, S. & Chen, S. 2018*a* Kinetic energy transfer in compressible isotropic turbulence. *J. Fluid Mech.* **841**, 581–613.

Wang, J., Wan, M., Chen, S., Xie, C. & Chen, S. 2018*b* Effect of shock waves on the statistics and scaling in compressible isotropic turbulence. *Phys. Rev.* E **97**, 043108.

Wang, J., Wan, M., Chen, S., Xie, C., Zheng, Q., Wang, L.-P. & Chen, S. 2020 Effect of flow topology on the kinetic energy flux in compressible isotropic turbulence. *J. Fluid Mech.* **883**, A11.

Wang, J., Wang, L., Xiao, Z., Shi, Y. & Chen, S. 2010 A hybrid numerical simulation of isotropic compressible turbulence. *J. Comput. Phys.* **229** (13), 5257–5279.

Wang, J., Yang, Y., Shi, Y., Xiao, Z., He, X.T. & Chen, S. 2013*a* Cascade of kinetic energy in three-dimensional compressible turbulence. *Phys. Rev. Lett.* **110** (21), 214505.

Wang, J., Yang, Y., Shi, Y., Xiao, Z., He, X.T. & Chen, S. 2013*b* Statistics and structures of pressure and density in compressible isotropic turbulence. *J. Turbul.* **14** (6), 21–37.

Watanabe, T. & Gotoh, T. 2007 Inertial-range intermittency and accuracy of direct numerical simulation for turbulence and passive scalar turbulence. *J. Fluid Mech.* **590**, 117–146.

Wu, K.-K., Chang, Y.-C., Chen, C.-H. & Chen, Y.-D. 2010 High-efficiency combustion of natural gas with 21–30 % oxygen-enriched air. *Fuel* **89** (9), 2455–2462.

Yasuda, T. & Vassilicos, J.C. 2018 Spatio-temporal intermittency of the turbulent energy cascade. *J. Fluid Mech.* **853**, 235–252.